

Ductile fracture of high strength steels with morphological anisotropy. Part II: Nonlocal micromechanics-based modeling

Julien Leclerc^a, Matthieu Marteleur^b, Marie-Stéphane Colla^b, Thomas Pardoen^b, Ludovic Noels^{a,*}, Van-Dung Nguyen^a

^a*Computational & Multiscale Mechanics of Materials, Department of Aerospace and Mechanical Engineering, University of Liège, B-4000 Liège, Belgium*

^b*Institute of Mechanics, Materials and Civil Engineering, UCLouvain, B-1348 Louvain-la-Neuve, Belgium*

Abstract

The ductile fracture behavior of a high strength steel is addressed in this two-part study using a micromechanics-based approach. The objective of Part II is to propose, identify, and validate a numerical model of ductile fracture based on the Gurson-Tvergaard-Needleman model. This model is enhanced by the Nahshon-Hutchinson shear modification in combination with the Thomason coalescence criterion within a fully nonlocal form and relying on a damage-to-crack transition technique. The material model involves parameters of different nature either related to the micro-mechanics of porous materials or to semi-empirical formalisms. The void nucleation model and elastoplastic behavior have been developed and identified in Part I. The other parameters are identified in this part using inverse modeling based on both the numerical results of void cell simulations and the experimental measurements. The model is shown to adequately predict the effect of stress triaxiality and Lode parameter on the fracture strain as well as the fracture anisotropy. While the cup-cone and slant fracture paths in the round bars and in the plane strain specimens, respectively, cannot be captured using the pure continuum approach, the damage-to-crack transition framework reproduces these experimental observations.

Keywords: Ductile fracture, Gurson, Thomason, Cohesive Band Model

1. Introduction

Ductile fracture is the most common type of failure in metallic structures. The prediction of ductile fracture is crucial for structural optimization and design. An extensive number of studies has been devoted in the literature to predict this fracture mode under a large range of stress states for more than 5 decades now. Nevertheless the capabilities of numerical models are consistently challenged by the increasing complexity of the constitutive models and the number of parameters when dealing with complex failure scenarios. This involves complex loading paths, shear failure modes - transition from flat to slant paths in particular, length scale effect, microstructure anisotropy, and damage-to-crack transition. Our work focuses on using a model relying as much as possible on micromechanics and physical grounds while

*Corresponding author, Phone: +32 4 366 48 26, Fax: +32 4 366 95 05
Email address: L.Noels@ulg.ac.be (Ludovic Noels)

considering several empirical simplifications in order to maintain an acceptable computational complexity.

The material investigated in this study is a high strength steel (HSS), which was received as hot forged hollow cylindrical pieces. In the companion paper - Part I [1] of the work, microstructural analyses of samples taken at various locations in the cylinders did not show heterogeneities along the thickness length. A strong anisotropy on the fracture strain was however found, due to the morphological anisotropy of the MnS inclusions, but with no significant plastic anisotropy. A test campaign conducted under different stress states characterized by the stress triaxiality and Lode parameter, and under different morphological directions, was presented. Part I divulged the first step in the modeling effort with the determination of the elastoplastic behavior and with the development and the identification of an anisotropic void nucleation law that captures the morphological anisotropy.

The literature provides many options to build a predictive model for ductile fracture, see the comprehensive reviews in [2, 3, 4, 5] and references therein. The ductile fracture models follow either phenomenological or micromechanical approaches.

From a phenomenological point of view, the fracture starts when a damage indicator, which is phenomenologically constructed, exceeds a certain critical value. On the one hand, the coupled models (so-called Continuum Damage Mechanics - CDM) have been developed within a thermodynamically consistent framework. The material degradation is characterized by a damage variable related to the irreversible internal state evolution of the material microstructure. This class of models has been continuously developed and widely used, see *e.g.* the works by [6, 7, 8, 9, 10, 11]. The difficulty with these models is to link the parameters to the physical mechanisms. In contrast to coupled models, on the other hand, uncoupled models (so-called fracture criteria) assume that the damage indicator is independent of the material elastoplastic behavior, see *e.g.* the works by [12, 13, 14, 15]. In this class of models, the damage indicator is generally expressed by a cumulative function along the loading paths, *e.g.* an integral with respect to the equivalent plastic strain, of a function of the stress state. Because of their simplicity, the uncoupled models have been increasingly developed, especially for industrial applications [5]. However, the uncoupled models can lead to erroneous predictions of the post-damage behavior as the damage indicator does not interact with the material behavior.

Micromechanical models constitute the alternative approach. The models can sometimes be sophisticated, leading to additional numerical complexity, including in their implementation, as compared to CDM models. They rely on a description as realistic as possible of the ductile fracture processes of nucleation, growth, and coalescence of voids. The most popular micromechanical ductile fracture model was pioneered by Gurson [16], who introduced the void volume fraction into the macroscopic yield criterion to account for the material degradation; this introduction was based on an upper bound analysis of a spherical void embedded in an elastic-perfectly plastic matrix. This original form of the Gurson model was further extended to take into account different aspects: a better representation of the void growth and coalescence phases in the so-called Gurson-Tvergaard-Needleman (GTN) model [17, 18]; the introduction of void nucleation [19]; the effects of the void shape [20, 21, 22], void size [23], or again void rotation [24]; the plastic anisotropy [25, 26]; and the shear effect [27, 28]. Although the predictive capability of the micromechanical model was improved, very few of the extensions mentioned above, at the exception of the GTN model, were applied to large

scale structural modeling due to their numerical complexity.

The GTN model suffers from some limitations. On the one hand, the GTN model alone does not correctly predict fracture under low stress triaxiality. This limitation was partly resolved by modifying the void evolution law with a shear modified term as suggested by Nahshon and Hutchinson [27] in the so-called GTN-NH model. This shear modified term accounts for the effect of the Lode parameter at low triaxiality. On the other hand, although the GTN-NH model provides a complete computational methodology for all stages of void evolution, its description of void coalescence remains phenomenological: a critical value of the porosity is used to predict the onset of void coalescence beyond which the porosity growth rate is artificially accelerated through an effective porosity. This phenomenological void coalescence model does not provide a realistic description of the void coalescence [29], which motivates the use of micromechanics-based coalescence models as pioneered by [30, 31] with the so-called Thomason model. This Thomason model considers that coalescence starts when plastic deformation localizes in the ligaments between neighboring voids. After this transition, the plastic deformation is governed by a plastic flow completely different than the one during the void growth phase and is correctly modeled neither with the GTN model, nor with the GTN-NH model. The Thomason model was further extended to better represent the internal necking coalescence process, see *e.g.* the works by [29, 32, 33, 34]. The Thomason model and its extended forms can be used either to detect the onset of coalescence while using the GTN or GTN-NH frameworks [35, 36], or as an additional yield surface governing the coalescence process, see *e.g.* the works by [29, 37, 25, 38, 39, 40]. While the Thomason model captures coalescence by necking, shear-driven coalescence can also be accounted for in the micro-mechanical model by introducing an extra yield surface governed by the maximum shear stress [40]. Note also that the GTN-NH model does not include the void shape effect requiring the fitting of some adjustment parameters, see [20, 21].

When dealing with problems involving material strain softening, loss of ellipticity at the onset of softening results in strain localization within a band whose thickness depends on the mesh size. Consequently, the boundary value problem formulated in a standard local continuum becomes ill-posed and the finite element unique solution does not exist [41]. Nonlocal formulations, in which intrinsic lengths are incorporated into the constitutive relations, accounting for interactions between neighboring material points [42, 43, 44], recover solution uniqueness. In particular, several nonlocal versions of the GTN frameworks can be found in the literature, see *e.g.* [45, 46, 47, 48, 49, 50, 40, 39]. The implicit gradient enhanced nonlocal formulation pioneered in [51] is employed in this work since it can be more easily integrated into a standard finite element formulation as considered in [39]. Besides, the various GTN frameworks have been shown to successfully predict the cup-cone and slant fracture paths in round bars and plane strain specimens, respectively, either by considering a strain controlled void nucleation function [52, 53, 46] or by combining the yield surfaces of the GTN with a shear-driven coalescence model [40]. Recently, these complex fracture patterns were also captured by using a damage-to-crack transition framework in which the creation of the free surfaces at coalescence produces such complex fracture patterns [39]. This damage-to-crack transition framework is employed in this work.

In this paper, designated as Part II, the numerical modeling of the fracture behavior of the HSS material is investigated using the micromechanical approach, focusing on micromechanical grounds as much as possible while maintaining some empirical simplifications in order to

obtain an efficient predictive model with an acceptable computational cost. As a result, the GTN-NH/Thomason model developed in the work [39] is chosen. In this model, the diffuse plasticity corresponding to the growth of voids is described by the GTN-NH model while the localized plasticity corresponding to the coalescence of voids is described by the Thomason model derived from the Thomason coalescence condition. To resolve the mesh-dependency issue in the pre-coalescence stage, when dealing with material softening, the nonlocality of the porosity is considered using the implicit gradient enhanced nonlocal model [51]. However, the ligament ratio can localize in a single-element thick band during the post-coalescence stage for such a nonlocal model, which could be prevented by considering a multiple-nonlocal variable framework as in [40] or by considering, alongside the nonlocal GTN-NH/Thomason model, a damage-to-crack transition framework. Such a framework was developed in [39] in the context of the discontinuous Galerkin method and is also considered to model the crack propagation during the post-coalescence stage of voids through a cohesive band model [54], hence avoiding the mesh dependency issue during the whole failure process. In this damage-to-crack transition framework, cracks are inserted at the onset of the coalescence, while the local version of the Thomason model is considered instead of using a fully nonlocal version of the GTN-NH/Thomason model to govern the crack opening. Since a mixed nonlocal/local constitutive law is used in the damage-to-crack transition framework, an additional parameter, so-called cohesive band thickness, plays the role of the characteristic length during crack propagation, ensuring the mesh-independence during that final stage as well.

Since the elastoplastic behavior and the void nucleation law were identified in the companion paper [1], this Part II focuses on the identification of the remaining parameters of the GTN-NH/Thomason model in both the nonlocal form and in the damage-to-crack transition framework, and on the validation of the full model:

- Since the GTN-NH/Thomason model derives from a micromechanical basis, several of its adjustment parameters can be calibrated using void cell simulations, see *e.g.* [55, 56, 29, 57, 58]. This calibration process is based on the solutions of two unit cell problems: (i) a unit cell containing a discrete void embedded in a matrix obeying the constitutive behavior of the undamaged material and (ii) a unit cell obeying the GTN constitutive behavior and with the same initial void volume fraction. Both unit cells are subjected to the same loading conditions and the parameters of the GTN model can be calibrated by minimizing the differences between their response prior to the onset of void coalescence. However, this identification approach assumes the macroscopic strain equivalence and disregards the energy dissipation consistency, which is considered to couple the scales when developing the micro-mechanical models. In this paper the void growth and void coalescence parameters of the GTN-NH/Thomason model are calibrated using void cell simulations by postulating the plastic dissipation equivalence.
- The values of the characteristic nonlocal length and of the cohesive band thickness are taken from microstructure characterization to assess whether these lengths are indeed related to the physical length scales at play.
- Finally, the shear enhanced contribution is identified using inverse modeling.

This Part II is organized as follows. In Section 2, the nonlocal GTN-NH/Thomason model and the associated damage-to-crack transition technique developed in the work [39]

are recalled. In Section 3, the identification of the GTN-NH/Thomason parameters based on void cell simulations and of the remaining parameters are detailed. Once all material parameters of the nonlocal GTN-NH/Thomason model are available, the experimental tests presented in the companion paper [1] are simulated and the results comparison is conducted in Section 4. The damage-to-crack transition framework is considered in Section 5 to model the crack propagation. Finally, the problem of stable crack propagation is studied in Section 6 on a compact test (CT) specimen, both numerically and experimentally, in order to validate the model characteristic lengths.

2. Porous plasticity model

The nonlocal coupled GTN-NH/Thomason model and the damage-to-crack transition framework essentially developed in the work [39] are summarized in this section.

2.1. Nonlocal GTN-NH/Thomason model

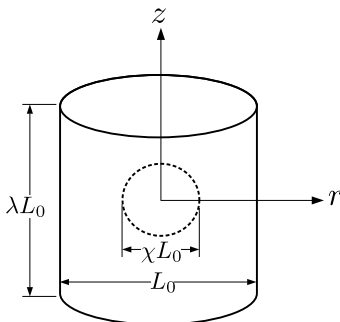


Figure 1: The geometrical description of a spherical void embedded in a cylindrical unit cell: the cell aspect ratio λ , the ligament ratio χ , and the porosity $f_V = \frac{2\chi^3}{3\lambda}$.

The constitutive model is specified within a finite strain setting as the evolution of the first Piola-Kirchhoff stress tensor (denoted by \mathbf{P}) in terms of the deformation gradient tensor (denoted by \mathbf{F}) and a set of internal variables \mathbf{Z} to capture the history and path dependencies as

$$\mathbf{P} = \mathfrak{P}(\mathbf{F}, \mathbf{Z}), \text{ and evolution laws for } \mathbf{Z}. \quad (1)$$

The behavior of the pristine matrix obeys the J_2 flow theory. The underlying damage mechanism is assimilated to the growth and coalescence of voids under the assumption (for the treatment of coalescence) that the voids are periodically distributed in the matrix and stay spherical during the entire loading process. As a result, the geometrical state of a void is fully described by three parameters: the porosity (denoted by f_V), the void ligament ratio (denoted by χ), and the void aspect ratio (denoted by λ) as illustrated in Fig. 1. These three parameters are related by the following relationship

$$\chi = \left(\frac{3}{2} f_V \lambda \right)^{1/3}. \quad (2)$$

A rate-independent, isotropic elastic, and isothermal behavior is assumed. Additionally, an inelastic deformation does not affect the elastic material response.

The nonlocal GTN-NH/Thomason model is based on two solutions: the void growth solution corresponding to a diffuse mode of plastic flow around the growing voids is governed by the GTN-NH model and the solution corresponding to the void coalescence phase by localized plasticity between voids is governed by the Thomason model. These two solutions are considered under the form of two distinct plastic yield functions supplemented by the evolution laws of the internal variables \mathbf{Z} : plastic deformation \mathbf{F}^p , mean yield stress of the matrix τ_y , porosity f_V , void ligament ratio χ , and void aspect ratio λ .

2.1.1. Elastic behavior

A multiplicative decomposition of the deformation gradient is supposed as

$$\mathbf{F} = \mathbf{F}^e \cdot \mathbf{F}^p, \quad (3)$$

where \mathbf{F}^e is its elastic part and \mathbf{F}^p is its plastic part. The elastic behavior is based on a hyperelastic formulation, in which the elastic potential is given by

$$\psi = \frac{K}{2} (\ln J^e)^2 + \frac{G}{4} \text{dev}(\ln \mathbf{C}^e) : \text{dev}(\ln \mathbf{C}^e), \quad (4)$$

where \mathbf{C}^e is the elastic right Cauchy strain tensor, $\text{dev}(\mathbf{A})$ represents the deviatoric part of an arbitrary second order tensor \mathbf{A} , $J^e = \det \mathbf{F}^e > 0$ is the elastic Jacobian, and K and G are respectively the bulk and shear moduli of the material. The first Piola-Kirchhoff stress tensor \mathbf{P} is estimated from the hyperelastic potential (4) under a purely elastic state (constant \mathbf{F}^p) as

$$\mathbf{P} = \frac{\partial \psi}{\partial \mathbf{F}} = K \mathbf{F}^{-T} \ln J^e + \mathbf{F}^e \cdot [G \mathbf{C}^{e-1} \cdot \text{dev}(\ln \mathbf{C}^e)] \cdot \mathbf{F}^{p-T}. \quad (5)$$

In terms of the elastic logarithmic strain measure, defined as $\mathbf{E}^e = \frac{1}{2} \ln \mathbf{C}^e$, Eq. (4) leads to the definition of the logarithmic stress measure $\boldsymbol{\tau}$, which is energetically conjugate to \mathbf{E}^e , as

$$\boldsymbol{\tau} = \frac{\partial \psi}{\partial \mathbf{E}^e} = K \text{tr}(\mathbf{E}^e) \mathbf{I} + 2G \text{dev}(\mathbf{E}^e), \quad (6)$$

where $\text{tr}(\mathbf{A})$ represents the trace of an arbitrary second order tensor \mathbf{A} . One can demonstrate that $\boldsymbol{\tau}$ is interpreted as the Kirchhoff stress represented in the elastic corotational space [59]. This stress measure relates to the first Piola-Kirchhoff stress tensor \mathbf{P} as a result of Eqs. (5, 6) through the following relation

$$\boldsymbol{\tau} = \mathbf{F}^{eT} \cdot \mathbf{P} \cdot \mathbf{F}^{pT}. \quad (7)$$

2.1.2. Yield functions

The corotational Kirchhoff stress tensor $\boldsymbol{\tau}$ is used as the driving stress in the yield functions. The yield function (denoted by Φ_{nl}) is selected among the GTN yield function (denoted by Φ_g) and the Thomason yield function (denoted by Φ_c) depending on the active mechanism of the void evolution, respectively either the growth phase or the coalescence phase. Mathematically, one considers

$$\Phi_{nl} = \max(\Phi_g, \Phi_c). \quad (8)$$

The void growth phase is governed by the GTN yield function Φ_g , which is expressed as

$$\Phi_g = \left(\frac{\tau_{\text{eq}}}{\tau_y} \right)^2 + 2\tilde{f}_V^* q_1 \cosh \left(\frac{3}{2} q_2 \frac{p}{\tau_y} \right) - q_1^2 \tilde{f}_V^{*2} - 1, \quad (9)$$

in which $\tau_{\text{eq}} = \sqrt{\frac{3}{2} \text{dev}(\boldsymbol{\tau}) : \text{dev}(\boldsymbol{\tau})}$ is the von Mises equivalent stress, $p = \frac{\text{tr}(\boldsymbol{\tau})}{3}$ is the pressure, q_1 and q_2 are two material constants, and \tilde{f}_V^* is the so-called yield porosity, whose evolution law is given as

$$\dot{\tilde{f}}_V^* = \begin{cases} \dot{\tilde{f}}_V & \text{during a nonlocal update,} \\ \dot{f}_V & \text{during a local update,} \end{cases} \quad (10)$$

where \tilde{f}_V denotes the nonlocal porosity. In the case of a nonlocal simulation without crack insertion, the yield porosity \tilde{f}_V^* is always updated from the nonlocal porosity \tilde{f}_V . However, when considering the damage-to-crack transition, since a local form of the GTN-NH/Thomason model governs the Cohesive Band Model, this requires to shift from a nonlocal formalism to a local one at the interface Gauss points where the crack is inserted. The porosity used in the yield surface ought to remain continuous at crack insertion. To this end, the yield porosity \tilde{f}_V^* is incremented from the increment in the nonlocal porosity \tilde{f}_V before crack insertion and from the increment in the local porosity f_V beyond crack insertion [39].

The void coalescence stage is governed by the Thomason yield function Φ_c , which is expressed as

$$\Phi_c = \frac{2}{3} \frac{\tau_{\text{eq}}}{\tau_y} + \frac{|p|}{\tau_y} - C_{\text{Tf}}(\chi), \quad (11)$$

with C_{Tf} being the load concentration factor

$$C_{\text{Tf}}(\chi) = (1 - \chi^2) \left[\alpha \left(\frac{1}{\chi} - 1 \right)^2 + \frac{\beta}{\sqrt{\chi}} \right], \quad (12)$$

where α and β are material constants. Following [29], α is calibrated as a function of the representative strain hardening exponent of the matrix and $\beta = 1.24$. An increase of χ results in a shrinkage of the yield surface, leading to a reduction of the stress carrying capability. The Thomason yield function (11) is extended from the Thomason criterion [30, 31] which assumes an axisymmetric configuration [3]. If the stress state is not axisymmetric, the prediction could be erroneous since this formulation does not account for the Lode effect. Despite of this limitation, the Thomason yield function (11) was applied to arbitrary orientations of the localization band in order to model void coalescence by internal necking at moderate and high stress triaxialities showing good predictions [37, 60, 25, 61] and it is thus used as such in this work. However, in order to gain accuracy, an extension of the Thomason condition accounting for the Lode effect was suggested in [40], in which an extended version based on the maximum principal stress was investigated. The Thomason yield function (11) exhibits singularities at $p = 0$ (under pure shear) and at $\tau_{\text{eq}} = 0$ (under hydrostatic pressure). These corners are rounded using an interpolation-based regularization scheme [38] in order to produce a smooth normal evolution along the yield surface.

The nonlocal porosity \tilde{f}_V considered in Eq. (10) is estimated from its local counterpart f_V through the resolution of an additional Helmholtz-type boundary value problem [51]

$$\dot{\tilde{f}}_V - l^2 \Delta_0 \dot{\tilde{f}}_V = \dot{f}_V, \quad (13)$$

where l is the nonlocal length and Δ_0 is the Laplace operator with respect to the reference configuration. The differential equation (13) is completed by a natural boundary condition [51]. It is noted that Eq. (13) is often written without using the incremental form in the literature. When the initial porosity is uniformly distributed and the damage-to-crack transition is not considered, the two formulations, with and without time derivatives, are equivalent. However if a nonuniform initial porosity is prescribed, the use of the rate form as considered in Eq. (13) avoids the artificial smoothing arising because the additional Helmholtz-type Eq. (13) is not initially satisfied. Besides, when considering the damage-to-crack transition, as a result of the natural boundary condition at the evolving free surface created by the crack opening during loading, the formulation with time derivatives does not lead to a jump of the normal component of the nonlocal flux. Indeed, in the formulation without time derivatives, such a jump appears at these crack interfaces at the insertion time since the nonlocal variable starts becoming discontinuous, leading to the numerical convergence issues. As a result, this study considers the formulation with time derivatives in which the damage-to-crack transition can be smoothly carried out [39]. Moreover, since a local form of the GTN-NH/Thomason model governs the Cohesive Band Model, this requires to shift from a nonlocal formalism to a local one at the interface Gauss points where the crack is inserted. This transition is achieved by considering the increment of the yield porosity used in the yield surface (9), which comes either from the nonlocal form before crack insertion or from the local form beyond crack insertion, see Eq. (10). It is thus more natural to consider incremental form for the Helmholtz type equation as well. The additional Helmholtz-type boundary value problem (13) is solved monolithically with the classical mechanical equations in a fully coupled form. The implementation details can be found in [39].

The use of the Laplace operator with respect to the reference configuration in Eq. (13) leads to a so-called material nonlocal formulation. The Laplace operator could also have been considered with respect to the current configuration, leading to a so-called spatial nonlocal formulation [62]. Mathematically, a material nonlocal formulation is always equivalent to a spatial nonlocal formulation but the corresponding nonlocal lengths are neither the same nor proportional since their relationship evolves as a function of the state of the deformation gradient. On the one hand, the numerical study performed in [62] shows that a spatial nonlocal formulation with a constant spatial length parameter cannot resolve pathological mesh dependence, while a material nonlocal formulation provides all the targeted regularization features. On the other hand, a material nonlocal formulation facilitates the numerical implementation since the resulting stiffness matrix does not require an additional geometrical term, motivating the choice of a material nonlocal formulation.

The constitutive material law is integrated following an incremental and fully implicit scheme [39]. In order to remove surface vertices at the intersection between the two yield functions specified by Eq. (8) and to ensure a unique plastic flow normal during each time step, the onset of coalescence is checked after every time step, and when activated, the model switches to the coalescence yield surface for the rest of the loading history.

2.1.3. Evolution laws

Plastic deformation gradient \mathbf{F}^P : an associative and irrotational plastic flow¹ is assumed, resulting into

$$\mathbf{D}^P = \dot{\mathbf{F}}^P \cdot \mathbf{F}^{P-1} = \dot{\Lambda} \frac{\partial \Phi_{nl}}{\partial \boldsymbol{\tau}}, \quad (14)$$

where \mathbf{D}^P denotes the plastic strain rate and Λ is the plastic multiplier.

Mean yield stress of the matrix τ_y : the evolution law for τ_y is first expressed through ε_m , the so-called mean equivalent plastic strain of the matrix, following an explicit hardening law:

$$\tau_y = \tau_y(\varepsilon_m). \quad (15)$$

The evolution law for ε_m is then determined under the assumption that the rate of current plastic work is equal to the rate of plastic work in the matrix [16, 17, 18]

$$\boldsymbol{\tau} : \mathbf{D}^P = (1 - f_{V0}) \tau_y \dot{\varepsilon}_m, \quad (16)$$

where $\boldsymbol{\tau} : \mathbf{D}^P$ characterizes the total plastic dissipation and f_{V0} is the initial porosity.

Local porosity f_V : different contributions are accounted for, following

$$\dot{f}_V = \underbrace{(1 - f_V) \text{tr}(\mathbf{D}^P)}_{\dot{f}_{V\text{gr}}} + \dot{f}_{V\text{nu}} + \underbrace{k_\omega (1 - \zeta^2) f_V \frac{\text{dev}(\boldsymbol{\tau}) : \mathbf{D}^P}{\tau_{\text{eq}}}}_{\dot{f}_{V\text{sh}}}, \quad (17)$$

where the first term $\dot{f}_{V\text{gr}}$ (so-called growth term) is the usual term associated to the plastic incompressibility of the matrix [17, 18]; the second term $\dot{f}_{V\text{nu}}$ (so-called void nucleation term) is the contribution of new voids nucleated due to particle debonding or cracking [19]; and the third term $\dot{f}_{V\text{sh}}$ (so-called shear term) corresponds to an effective change of porosity due to void deformation and reorientation occurring under low stress triaxiality and shear-dominated distortions [27]. In the shear term, k_ω is a material constant [27] and ζ is the Lode parameter defined by

$$\zeta = \frac{27 J_3}{2 \tau_{\text{eq}}^3}, \quad (18)$$

where $J_3 = \det(\text{dev}(\boldsymbol{\tau}))$.

Void aspect ratio λ : following [32], one has

$$\dot{\lambda} = \kappa \dot{\varepsilon}_m \lambda, \quad (19)$$

where κ is a user parameter, so-called void spacing growth factor, which depends on the distribution of voids: $\kappa = 1.5$ for a periodic distribution under tension, $\kappa = 0$ for a random distribution, and $0 \leq \kappa \leq 1.5$ for a clustered distribution.

¹For isotropic elastoplastic materials, when using the decomposition of the deformation gradient following Eq. (3), it is widely assumed [63], without loss of generality, that the plastic flow is irrotational –*i.e.* the plastic spin vanishes– since this simplifies the developments.

Void ligament ratio χ : it is assumed that the voids remain spherical as considered in [38] and, considering the yield porosity \tilde{f}_V^* in Eq. (2), one has $\chi = \left(\frac{3}{2}\tilde{f}_V^*\lambda\right)^{1/3}$, or, in a rate form,

$$\dot{\chi} = \frac{\chi}{3} \left(\frac{\dot{\tilde{f}}_V^*}{\tilde{f}_V^*} + \frac{\dot{\lambda}}{\lambda} \right), \quad (20)$$

in which either the nonlocal or the local formalism for the Thomason yield surface (11) can be embedded according to the update of \tilde{f}_V^* in Eq. (10). We however note that, during the coalescence stage, the nonlocality of χ is not always enough to prevent the localization to occur in a single-element thick band as it will be shown in Section 4. This mesh dependency can be prevented by considering a multiple-nonlocal variable framework as in [40] or by introducing a crack through a Cohesive Band Model as discussed here below. When $\chi = 1$, the Thomason yield function (11) shrinks to a zero stress state and the load carrying capacity is totally lost. In order to avoid high mesh distortions, the value of χ is limited at each integration point by a critical value smaller and close enough to 1. The effect of this tolerance has a negligible contribution to the internal forces.

2.2. Damage-to-crack transition

Alongside the nonlocal coupled GTN-NH/Thomason model described above, which provides a complete computational methodology for all stages of void evolution until final fracture, the damage-to-crack transition framework developed in [39] is an interesting alternative. This framework introduces real discontinuities and can capture complex failure modes. Here, crack surfaces are introduced in the mechanical problem through a cohesive band model (CBM) as soon as the void coalescence process has started.

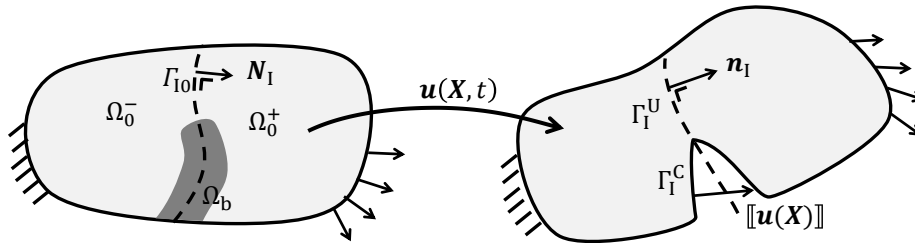


Figure 2: Discontinuity surface Γ_{10} embedded in a fictitious cohesive band Ω_{b0} in the reference configuration (left) and in the current configuration (right). The discontinuity separates the volume Ω_0 into two parts Ω_0^- and Ω_0^+ .

Let us consider a discontinuity Γ_{10} embedded in a body Ω_0 as illustrated in Fig. 2, the volume Ω_0 is divided into two parts Ω_0^- and Ω_0^+ , with the unit normal vector in the reference configuration (denoted by \mathbf{N}_I) at each point of Γ_{10} oriented towards Ω_0^+ . At each material point $\mathbf{X} \in \Gamma_{10}$, one can define the jump and the mean operators respectively by

$$\llbracket \bullet \rrbracket = \bullet^+ - \bullet^- \quad \text{and} \quad \langle \bullet \rangle = \frac{1}{2} (\bullet^+ + \bullet^-), \quad (21)$$

that link arbitrary variables \bullet^+ and \bullet^- from both sides of Γ_{10} . In general, the general form of a cohesive law at a material point $\mathbf{X} \in \Gamma_{10}$ can be expressed as

$$\mathbf{T} = \mathfrak{T} (\llbracket \mathbf{u} \rrbracket, \mathbf{F}^+, \mathbf{F}^-, \mathbf{N}_I; \mathbf{Z}_I), \quad (22)$$

where \mathbf{T} is the cohesive traction, \mathbf{u} is the displacement field, \mathbf{F}^+ and \mathbf{F}^- are respectively the deformation gradient tensors from both sides of Γ_{I0} , and \mathbf{Z}_I is a vector of internal variables which is used to model the history-dependency.

Here, the cohesive law described in Eq. (22) is derived using the Thomason model following [39]. Prior to crack insertion, on Γ_I^U , Eq. (22) can be written as

$$\mathbf{T} = \langle \mathbf{P} \rangle \cdot \mathbf{N}_I, \quad (23)$$

in which \mathbf{P}^- , \mathbf{P}^+ in $\langle \mathbf{P} \rangle$ are estimated by Eq. (1). After the crack insertion, on Γ_I^C , Eq. (23) still holds but \mathbf{P}^- , \mathbf{P}^+ are respectively estimated using the underlying constitutive law (1) from \mathbf{F}_b^- and \mathbf{F}_b^+ , so-called band deformation gradient tensors, instead of \mathbf{F}^- and \mathbf{F}^+ . Prior to the crack insertion, one has $\mathbf{F}_b^\mp = \mathbf{F}^\mp$, and after the crack insertion, \mathbf{F}_b^\mp are enriched with the jump of the displacement field as

$$\dot{\mathbf{F}}_b^\mp = \dot{\mathbf{F}}^\mp + \frac{[[\dot{\mathbf{u}}]] \otimes \mathbf{N}_I}{h_b} + \frac{1}{2} \nabla_{0I} \otimes [[\dot{\mathbf{u}}]], \quad (24)$$

where h_b is the thickness of the cohesive band which controls the total dissipated energy, and ∇_{0I} is the gradient operator projected onto the crack surface. The last term in Eq. (24) represents the variation of the displacement jump $[[\mathbf{u}]]$ along the crack surface, but is herein omitted. As the cracks are inserted at the onset of the coalescence, the predictor of the Thomason yield condition, *i.e.* $\Phi_c \geq 0$, acts as the criterion of the crack insertion. Once a crack is inserted, the local form of the Thomason model is used at these interface Gauss points to govern the plastic flow during the crack propagation. Indeed, on the one hand the cohesive band model does not suffer from mesh dependency in a local form, and on the other hand, physically, the neighboring elements are subjected to an elastic unloading while the damaging process concentrates within the cohesive band, which cannot be captured by considering a nonlocal formulation spanning the cohesive band and the neighboring elements. Besides, the void evolution is also blocked on the neighboring volume elements (but not the plastic flow), in order to favor elastic unloading instead of further volume softening. Consequently, the damage-to-crack transition at a material point $\mathbf{X} \in \Gamma_{I0}$ is made through two simultaneous transitions:

- (i) From the deformation gradient tensor \mathbf{F}^\mp to the band deformation gradient tensor \mathbf{F}_b^\mp ; and
- (ii) From the nonlocal GTN-NH model to the local Thomason model by considering the incremental update in Eq. (10).

Although a local constitutive law is used during crack propagation, cohesive zone and cohesive band models do not suffer from mesh-dependency, since a finite amount of energy is dissipated during the crack opening. In the case of the cohesive band model, this amount depends on the cohesive band thickness h_b . We note that the loss of ellipticity is sometimes met well before the onset of coalescence [64] justifying the need to consider the nonlocal form of the GTN-NH model to regularize the problem in that regime as well.

The damage-to-crack transition is implemented in the framework of the discontinuous Galerkin method, see [39] for details. The use of the cohesive band model in the damage-to-crack framework is more advantageous compared to the use of the conventional cohesive zone

model since it allows accounting for the in-plane deformation, hence for the stress triaxiality effect, and since it does not need the definition of a traction-separation law. However an additional parameter, the cohesive band thickness h_b , needs to be calibrated.

2.3. Model summary

The parameters of the nonlocal GTN-NH/Thomason model and of the damage-to-crack transition to be identified are summarized in Tab. 1. The numerical integration follows a predictor-corrector scheme as detailed in [39]. In the following, the GTN/Thomason model is used to mention the GTN-NH/Thomason model in the absence of the shear-induced void growth term in the void evolution, *i.e.* when $k_\omega = 0$.

Table 1: Material parameters to be calibrated.

| | |
|----------------------------|---|
| K | Bulk modulus (see Eq. (4)) |
| G | Shear modulus (see Eq. (4)) |
| f_{V0} | Initial porosity |
| χ_0 (or λ_0) | Initial ligament ratio (or initial spacing ratio) |
| q_1, q_2 | GTN coefficients (see Eq. (9)) |
| α, β | Thomason load factors (see Eq. (12)) |
| l | Nonlocal length (see Eq. (13)) |
| $\tau_y(\varepsilon_m)$ | Yield stress function (see Eq. (15)) |
| k_ω | Shear-induced growth factor (see Eq. (17)) |
| \dot{f}_{Vnu} | Nucleation law (see Eq. (17)) |
| κ | Void spacing growth factor (see Eq. (19)) |
| h_b | Cohesive band thickness (see Eq. (24)) |

3. Parameters identification for the nonlocal GTN-NH/Thomason model

The parameters of the nonlocal GTN-NH/Thomason model reported in Tab. 1 can be divided into different categories:

- (i) The elastoplastic parameters are the following: the elastic compressibility and shear moduli, respectively K and G , and the hardening law $\tau_y = \tau_y(\varepsilon_m)$, which is expressed under the following form as proposed in Part I [1]²:

$$\tau_y(\varepsilon_m) = \begin{cases} \tau_y^0 + h\varepsilon_m & \text{if } \varepsilon_m \leq p_1 \\ \tau_{y1} \left(\frac{\varepsilon_m}{p_1} \right)^{n_1} & \text{if } p_1 < \varepsilon_m \leq p_2 \\ \tau_{y2} \left(\frac{\varepsilon_m}{p_2} \right)^{n_2} & \text{if } \varepsilon_m > p_2 \end{cases}, \quad (25)$$

where τ_y^0 is the initial yield stress, h , p_1 , p_2 , n_1 , and n_2 are the hadening parameters, and $\tau_{y1} = \tau_y^0 + hp_1$ and $\tau_{y2} = \tau_{y1} \left(\frac{p_2}{p_1} \right)^{n_1}$;

²For confidentiality reasons, the numerical values of these parameters were not provided.

- (ii) The porous-plasticity related parameters: f_{V0} , λ_0 , χ_0 , q_1 , q_2 , α , β , k_ω , κ , and the nucleation evolution law \dot{f}_{Vnu} ; and
- (iii) The characteristic lengths: the nonlocal length l and the cohesive band thickness h_b .

The elastoplastic parameters, the initial parameters of the void characteristics and the nucleation evolution law \dot{f}_{Vnu} , which corresponds to an anisotropic nucleation model to take into account fracture anisotropy and which remains to be validated in this Part II, were calibrated in Part I [1].

The correction constants α and β entering the coalescence limit load (12) of the Thomason model are obtained using the relationship established in [29] by fitting void cell simulations as

$$\alpha = 0.1 + 0.217n_2 + 4.83n_2^2 = 0.129 \text{ and } \beta = 1.24. \quad (26)$$

The value of n_2 is considered in the last equation because the onset of coalescence occurs at plastic strains usually much larger than p_2 as shown in Part I. The value of p_2 is close to the equivalent plastic strain at the onset of necking of the SRB specimens.

The nucleation term \dot{f}_{Vnu} was worked out in Part I [1] as an anisotropic nucleation law in order to capture the effect of the morphological anisotropy on the fracture strain as observed in the experimental tests. Its expression reads

$$\dot{f}_{Vnu} = \begin{cases} A_n \dot{\epsilon}_m & \text{once } \Phi_n \geq 0 \text{ has been met during the loading history,} \\ 0 & \text{otherwise,} \end{cases} \quad (27)$$

in which Φ_n is a void nucleation activation function whose expression is derived using the Beremin nucleation model [65] but which accounts for failure anisotropy and A_n is the parameter controlling the void nucleation intensity. This last term is expressed as a Gaussian distribution in the spirit of the Chu and Needleman pioneering model [19] and whose intensity is directional. The nucleation activation function Φ_n is defined under the assumption that the failure anisotropy originates from the porosity nucleation triggered by the fracture of the elongated MnS inclusions: when loaded in the longitudinal direction, the MnS inclusions nucleate by particle cracking, while, when loaded in the perpendicular direction, the porosity is generated by matrix/particle decohesion. Since the loading direction is considered in both the nucleation activation function Φ_n and the void nucleation intensity A_n , the void nucleation always occurs early in the loading process but the voids nucleate differently depending on the loading direction, from which the failure anisotropy emerges. The parameters of this anisotropic nucleation law and their corresponding calibrated values are reported in Part I of the work.

This section describes the identification of the remaining parameters. The values q_1 , q_2 , and κ are first calibrated using unit cell simulations. The values of the nonlocal length l and of the cohesive band thickness h_b are then provided by microstructure characterization. Finally, the value of k_ω is calibrated by fitting the fracture strain predicted by the numerical simulations with the experimental results obtained from the plane strain specimens in Part I.

3.1. Identification of q_1 , q_2 , and κ from unit cell simulations

This work proposes to use the plastic dissipation equivalence based on Eq. (16) to calibrate not only q_1 and q_2 but also κ . On the one hand, the void cell simulations under constant stress triaxiality are considered with a unit cell containing a discrete void and obeying the constitutive behavior of the undamaged matrix. On the other hand, the response driven by the plastic dissipation through Eq. (16) of a material point obeying to the GTN/Thomason model is considered. The plastic dissipation equivalence between the two models reads

$$\boldsymbol{\tau} : \mathbf{D}^p = \frac{1}{V_0} \int_{V_0} \boldsymbol{\tau}^{\text{local}} : \mathbf{D}^{\text{p,local}} dV_0, \quad (28)$$

where V_0 is the initial volume of the unit cell and where $\boldsymbol{\tau}^{\text{local}}$ and $\mathbf{D}^{\text{p,local}}$ are respectively the local corotational Kirchhoff stress tensor and the local plastic strain rate distributed over the unit cell. The left hand side term of Eq. (28) is the plastic dissipation rate of the GTN/Thomason model while the right hand side term of Eq. (28) is the average of the plastic dissipation rate over the unit cell. In terms of the hardening law of the undamaged matrix, $\tau_y(\varepsilon_m)$, described in Eq. (25), Eq. (28) can be rewritten as

$$(1 - f_{V0}) \tau_y(\varepsilon_m) \dot{\varepsilon}_m = \frac{1}{V_0} \int_{V_0} \tau_y(\varepsilon_m^{\text{local}}) \dot{\varepsilon}_m^{\text{local}} dV_0, \quad (29)$$

where f_{V0} is the initial porosity and $\varepsilon_m^{\text{local}}$ is the local equivalent plastic strain distributed over the unit cell.

Since the right hand side term of Eq. (29) is known from the unit cell solution, the value of ε_m and then the one of $\tau_y(\varepsilon_m)$ can be easily estimated by solving one nonlinear equation. Clearly, ε_m is the overall measure that quantifies the plastic dissipation in the entire unit cell. The macroscopic quantities (homogenized stress and porosity) evaluated from the unit cell simulation can then be expressed in terms of ε_m . As shown in the next section, the GTN/Thomason model under a constant stress triaxiality and driven by the plastic dissipation can be analytically solved leading to the corresponding solutions expressed in terms of ε_m . The values of q_1 , q_2 , and κ are then calibrated by minimizing the differences between the porosity and macroscopic stress evolution with respect to ε_m , on the one hand, predicted by the unit cell simulations and, on the other hand, corresponding to the analytical predictions of the GTN/Thomason model at a material point. The plastic dissipation equivalence avoids considering a homogeneous unit cell simulation to evaluate the material response with the GTN/Thomason model.

3.1.1. Solution of the coupled GTN/Thomason model under constant stress triaxiality

The local form of the GTN/Thomason model described in Section 2.1 can be obtained by considering the local update $\dot{f}_V^* = \dot{f}_V$ in Eq. (10). In terms of the stress tensor $\boldsymbol{\tau}$, the yield surface Φ_{nl} following Eq. (8) depends only on the two invariants τ_{eq} and p . As a result, the plastic flow described in Eq. (14) can be rewritten as ³

$$\mathbf{D}^p = \dot{\Lambda} \left[\frac{\partial \Phi_{\text{nl}}}{\partial \tau_{\text{eq}}} \frac{3 \text{dev}(\boldsymbol{\tau})}{2 \tau_{\text{eq}}} + \frac{\partial \Phi_{\text{nl}}}{\partial p} \frac{\mathbf{I}}{3} \right]. \quad (30)$$

³The relations $\frac{\partial \tau_{\text{eq}}}{\partial \boldsymbol{\tau}} = \frac{3 \text{dev}(\boldsymbol{\tau})}{2 \tau_{\text{eq}}}$ and $\frac{\partial p}{\partial \boldsymbol{\tau}} = \frac{\mathbf{I}}{3}$ are used.

One can define respectively the volumetric plastic strain rate (denoted by $\dot{\epsilon}_v$) and the deviatoric plastic strain rate (denoted by $\dot{\epsilon}_d$) as

$$\dot{\epsilon}_v = \text{tr}(\mathbf{D}^p) = \dot{\Lambda} \frac{\partial \Phi_{\text{nl}}}{\partial p}, \text{ and} \quad (31)$$

$$\dot{\epsilon}_d = \sqrt{\frac{2}{3} \text{dev}(\mathbf{D}^p) : \text{dev}(\mathbf{D}^p)} = \dot{\Lambda} \frac{\partial \Phi_{\text{nl}}}{\partial \tau_{\text{eq}}}. \quad (32)$$

By eliminating $\dot{\Lambda}$ in the two equations above, the normality rule of the yield surface results in the following relationship

$$\dot{\epsilon}_d = \mathfrak{R} \dot{\epsilon}_v \text{ with } \mathfrak{R} = \frac{\partial \Phi_{\text{nl}}}{\partial \tau_{\text{eq}}} \left(\frac{\partial \Phi_{\text{nl}}}{\partial p} \right)^{-1}. \quad (33)$$

The stress triaxiality T is defined as the ratio between the pressure and the von Mises stress *i.e.* $T = \frac{p}{\tau_{\text{eq}}}$. Under constant positive stress triaxiality T , Eqs. (9, 11) can be respectively rewritten as

$$\Phi_g = X^2 + 2q_1 f_V \cosh(1.5q_2 T X) - q_1^2 f_V^2 - 1, \text{ and} \quad (34)$$

$$\Phi_c = X \left(\frac{2}{3} + T \right) - C_{\text{Tr}}(\chi), \quad (35)$$

where $X = \frac{\tau_{\text{eq}}}{\tau_y}$. Since the condition $\Phi_c < 0$ acts as a criterion for the void growth phase, one has the expression of \mathfrak{R} in Eq. (33) as

$$\mathfrak{R} = \begin{cases} \frac{2}{3q_1 q_2} \frac{X}{f_V \sinh(1.5q_2 T X)} & \text{if } \Phi_c < 0 \\ \frac{2}{3} & \text{otherwise} \end{cases} = \mathfrak{R}(X, f_V, \chi; T, q_1, q_2). \quad (36)$$

Moreover using Eqs. (34, 35), Eq. (8) results in the solution of X in terms of f_V and χ as

$$X = \begin{cases} \mathfrak{L}^{-1}(f_V; T, q_1, q_2) & \text{if } \Phi_c < 0 \\ \frac{C_{\text{Tr}}(\chi)}{T + \frac{2}{3}} & \text{otherwise} \end{cases} = X(f_V, \chi; T, q_1, q_2), \quad (37)$$

where the function \mathfrak{L}^{-1} is the inverse of the function \mathfrak{L} , the solution of Eq. (34), with

$$f_V = \frac{\cosh(1.5q_2 T X) - \sqrt{X^2 + \sinh^2(1.5q_2 T X)}}{q_1} = \mathfrak{L}(X; T, q_1, q_2). \quad (38)$$

With neither the nucleation of voids nor the shear-induced void growth terms in Eq. (17), the evolution laws of the internal variables followings Eqs. (14, 16, 17, 19, 20) can be rewritten as

$$\begin{cases} \dot{\epsilon}_d = \mathfrak{R} \dot{\epsilon}_v, \\ (1 - f_{V0}) \dot{\epsilon}_m = X (\dot{\epsilon}_d + T \dot{\epsilon}_v), \\ \dot{f}_V = (1 - f_V) \dot{\epsilon}_v, \\ \dot{\lambda} = \lambda \kappa \dot{\epsilon}_m \text{ and} \\ \dot{\chi} = \frac{\chi}{3} \left(\frac{\dot{f}_V}{f_V} + \kappa \dot{\epsilon}_m \right), \end{cases} \quad (39)$$

where the functions $\mathfrak{R} = \mathfrak{R}(X, f_V, \chi; T, q_1, q_2)$ and $X = X(f_V, \chi; T, q_1, q_2)$ are available from Eqs. (36, 37). As the problem is driven by the plastic dissipation, *i.e.* by $\dot{\varepsilon}_m$, Eqs. (39) can be rewritten as

$$\begin{bmatrix} \dot{\varepsilon}_v \\ \dot{\varepsilon}_d \\ \dot{f}_V \\ \dot{\lambda} \\ \dot{\chi} \end{bmatrix} = \begin{bmatrix} A \\ \mathfrak{R}A \\ (1 - f_V)A \\ \lambda\kappa \\ \frac{\chi}{3} \left[\frac{(1-f_V)A}{f_V} + \kappa \right] \end{bmatrix} \dot{\varepsilon}_m, \quad (40)$$

where

$$A = \frac{1 - f_{V0}}{X(\mathfrak{R} + T)}. \quad (41)$$

Equation (40) combined with Eqs. (36, 37) is solved by using an explicit Euler scheme with as initial solution the set $(\varepsilon_v = 0, \varepsilon_d = 0, f_V = f_{V0}, \lambda = \lambda_0, \text{ and } \chi = \chi_0)$ for the sake of simplicity. The step size is decreased until reaching a converged solution. This yields the solution of $X, \varepsilon_v, \varepsilon_d, f_V, \lambda,$ and χ as a function of the plastic dissipation driven by ε_m for a given set of material parameters $(f_{V0}, q_1, q_2, \text{ and } \kappa)$ without the need of considering the explicit form of the hardening law of the matrix described by Eq. (15).

The solution provides the true von Mises equivalent stress σ_{eq} as

$$\sigma_{\text{eq}} = \frac{\tau_{\text{eq}}}{J} = \frac{X\tau_y}{J}, \quad (42)$$

where $\tau_y = \tau_y(\varepsilon_m)$ is the hardening function, and where J is the Jacobian. Following Eq. (3), the Jacobian can be decomposed into an elastic part $J^e = \det \mathbf{F}^e$ and a plastic part $J^p = \det \mathbf{F}^p$, such that

$$J = J^e J^p. \quad (43)$$

Using Eq. (6) and the identity $\ln(\det \mathbf{A}) = \text{tr}(\ln \mathbf{A})$ valid for an arbitrary symmetrical second-order tensor \mathbf{A} , one has

$$p = K \ln(J^e) = TX\tau_y, \quad (44)$$

leading to

$$J^e = \exp\left(\frac{TX\tau_y}{K}\right). \quad (45)$$

From the definition $J^p = \det \mathbf{F}^p$, one has

$$\dot{J}^p = J^p \mathbf{F}^{p-T} : \dot{\mathbf{F}}^p = J^p \mathbf{F}^{p-T} : (\mathbf{D}^p \cdot \mathbf{F}^p) = J^p \text{tr}(\mathbf{D}^p) = J^p \dot{\varepsilon}_v, \quad (46)$$

leading to

$$J^p = \exp(\varepsilon_v), \quad (47)$$

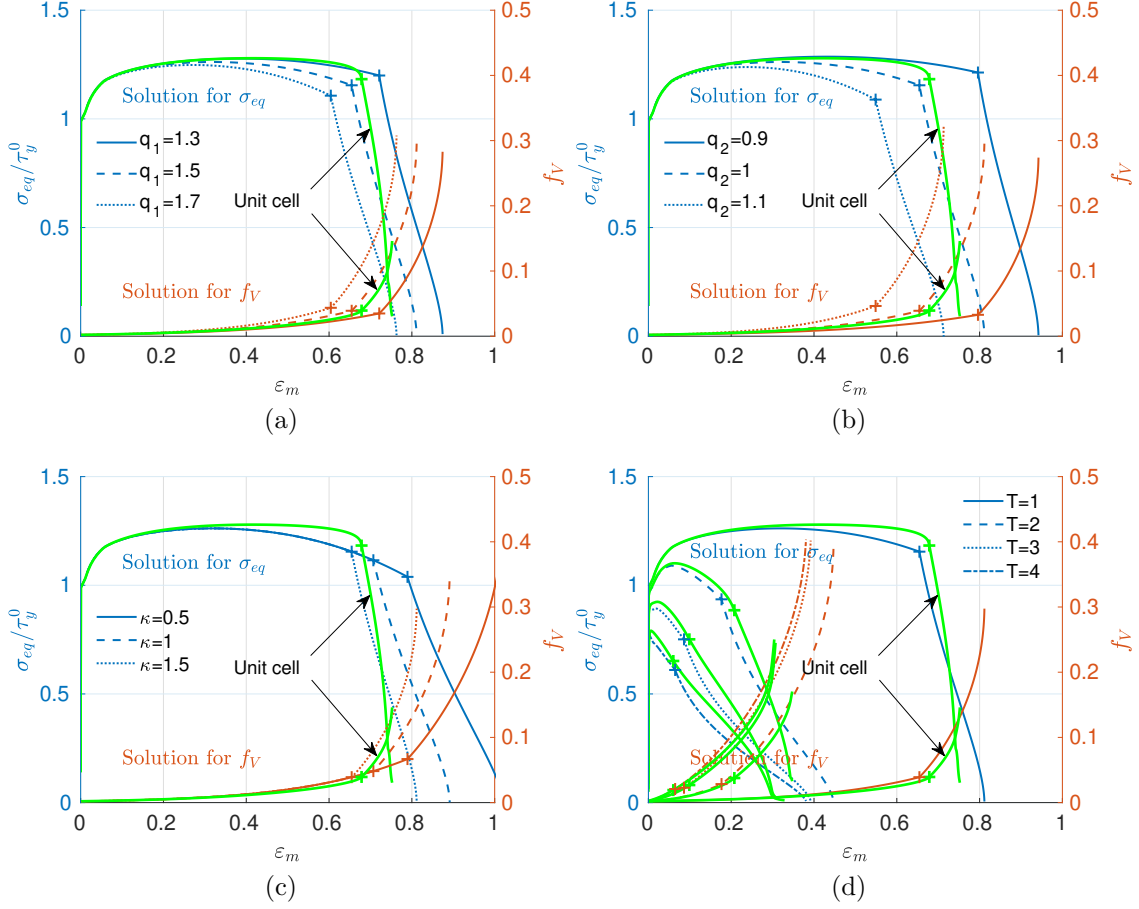


Figure 3: Solution of the GTN/Thomason model at constant stress triaxiality for an initial porosity $f_{V0} = 2 \times 10^{-3}$: (a) influence of q_1 for $q_2 = 1$, $\kappa = 1.5$, and $T = 1$, (b) influence of q_2 for $q_1 = 1.5$, $\kappa = 1.5$, and $T = 1$, (c) influence of κ for $q_1 = 1.5$, $q_2 = 1$, and $T = 1$, and (d) influence of T for $q_1 = 1.5$, $q_2 = 1$, and $\kappa = 1.5$. The symbol “+” indicates the onset of coalescence. The results obtained with the unit cell simulations, see Appendix A for details, are also reported.

since $J^p(\varepsilon_v = 0) = 1$. The calibration process only requires the solutions for σ_{eq} and for f_V , which can be expressed under their general forms:

$$\begin{cases} \sigma_{eq} &= \sigma_{eq}(\varepsilon_m; f_{V0}, T, q_1, q_2, \kappa), \text{ and} \\ f_V &= f_V(\varepsilon_m; f_{V0}, T, q_1, q_2, \kappa). \end{cases} \quad (48)$$

The two functions above cannot generally be expressed explicitly but result from the solution for X , ε_v , ε_d , f_V , λ , and χ for given material parameters.

Considering an initial porosity $f_{V0} = 2 \times 10^{-3}$, which is the onset of the nucleated porosity measured in Part I, the solutions of the GTN/Thomason model in terms of σ_{eq} and f_V versus ε_m as described in Eqs. (48), are shown in Fig. 3, in which the effects of the q_1 , q_2 , κ , and T are demonstrated. The description of the unit cell simulations is given in Appendix A while only the results are reported here. Since κ does not affect the void growth response but only the onset and post behavior of the coalescence stage, q_1 and q_2 are calibrated using the void

growth response while κ is calibrated using the data at the onset of coalescence obtained from the unit cell simulations.

3.1.2. Calibration methodology based on the dissipation equivalence

The results of the unit cell simulations before the onset of coalescence, *i.e.* for $\varepsilon_m \leq \varepsilon_{mc}^{\text{cell}}$, are considered as reference solutions to calibrate the values q_1 , q_2 of the GTN model while the data at the onset of coalescence are used to calibrate the value κ of the Thomason model.

Defining the dimensionless equivalent stress $Y = \frac{\sigma_{\text{eq}}}{\tau_y} = \frac{X}{J}$ where J is the Jacobian, the quantities $(Y^{\text{GTN}}, f_V^{\text{GTN}})$ and $(Y^{\text{cell}}, f_V^{\text{cell}})$ are used to indicate the corresponding solutions obtained with the GTN model and with the unit cell simulations, in which case the superscript “cell” refers to the homogenization of the unit cell problem. The errors on Y and f_V are respectively measured by the following functions

$$\begin{cases} \xi_Y &= \left| \frac{S_Y^{\text{cell}} - S_Y^{\text{GTN}}}{S_Y^{\text{cell}}} \right| = \xi_Y(f_{V0}, T, q_1, q_2), \text{ and} \\ \xi_f &= \left| \frac{S_f^{\text{cell}} - S_f^{\text{GTN}}}{S_f^{\text{cell}}} \right| = \xi_f(f_{V0}, T, q_1, q_2), \end{cases} \quad (49)$$

where S_Y (S_f) measures the surface limited by the curve $Y = Y(\varepsilon_m)$ ($f = f(\varepsilon_m)$) and the horizontal axis from the beginning ($\varepsilon_m = 0$) to the onset of coalescence $\varepsilon_m = \varepsilon_{mc}^{\text{cell}}$, and where “cell” and “GTN” denote a quantity estimated either by homogenization of the unit cell model or by the GTN model, respectively. The matrix plastic strain ε_m results from the energy equivalence (29) in the case of the “cell” solution. The two errors defined by Eqs. (49) can be combined, leading to an effective error as

$$\xi_{\text{eff}} = \sqrt{\frac{1}{2}\xi_Y^2 + \frac{1}{2}\xi_f^2} = \xi_{\text{eff}}(f_{V0}, T, q_1, q_2). \quad (50)$$

By performing the unit cell simulations for different values of f_{V0} ranging in the interval $[f_{V0\text{min}} \ f_{V0\text{max}}]$ and of T ranging in the interval $[T_{\text{min}} \ T_{\text{max}}]$, the accumulated error ξ_{acc} is defined by averaging the effective error given by Eq. (50) over the initial porosity and triaxiality ranges. One has

$$\xi_{\text{acc}}(q_1, q_2) = \frac{1}{f_{V0\text{max}} - f_{V0\text{min}}} \int_{f_{V0\text{min}}}^{f_{V0\text{max}}} \left(\frac{1}{T_{\text{max}} - T_{\text{min}}} \int_{T_{\text{min}}}^{T_{\text{max}}} \xi_{\text{eff}} dT \right) df_{V0}. \quad (51)$$

The values of q_1 , and of q_2 can be obtained by minimizing the accumulated error ξ_{acc} , according to

$$\min_{q_1, q_2} \xi_{\text{acc}}(q_1, q_2). \quad (52)$$

With $f_{V0} \in [1 \times 10^{-3} \ 2 \times 10^{-3}]$, $T \in [1 \ 4]$, the value of the accumulated error ξ_{acc} is shown in Fig. 4a. The optimum is found for $q_1 = 1.414$ and for $q_2 = 1$. These values of q_1 and q_2 are close to the typically utilized set $q_1 = 1.5$ and $q_2 = 1$, and the value of q_1 is close to the theoretical value $q_1 = 1.47$ derived by Perrin and Leblond [66] using a differential scheme.

The GTN/Thomason model described in Section 2.1 cannot capture the evolution of a true void in the unit cell. Instead, it is the evolution of an effective spherical void that leads

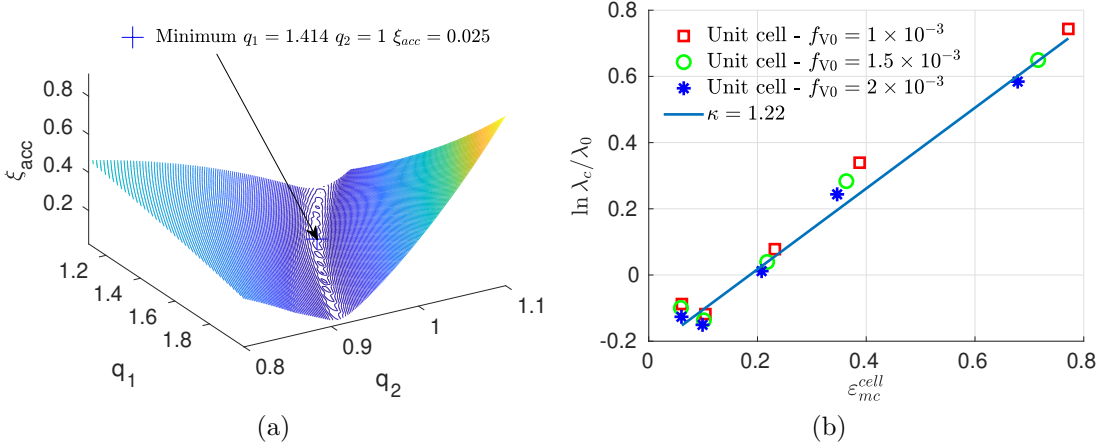


Figure 4: Calibration of q_1 , q_2 , and κ : (a) accumulated error ξ_{acc} in the (q_1, q_2) space in which the optimum point is marked and (b) curve fitting at the onset of coalescence for κ .

to the same constitutive behavior. As a result, the value of κ is calibrated using the values of σ_{eqc}^{cell} , f_{Vc}^{cell} , and ε_{mc}^{cell} obtained at the onset of coalescence from the unit cell simulations with different values of f_{V0} and of T . For this purpose, one assumes that the onset of coalescence occurs at $\Phi_c = 0$ where Φ_c is given by Eq. (35), leading to an estimation of the void ligament ratio at the onset of coalescence χ_c through the following equation

$$\left(\frac{2}{3} + T\right) \frac{J_c \sigma_{eqc}^{cell}}{\tau_y(\varepsilon_{mc}^{cell})} - C_{Tf}(\chi_c) = 0, \quad (53)$$

where J_c is the Jacobian at $\varepsilon_m = \varepsilon_{mc}^{cell}$. Using Eq. (53), χ_c can be easily deduced from

$$\chi_c = C_{Tf}^{-1} \left(\left(\frac{2}{3} + T\right) \frac{J_c \sigma_{eqc}^{cell}}{\tau_y(\varepsilon_{mc}^{cell})} \right), \quad (54)$$

where C_{Tf}^{-1} denotes the inverse function of C_{Tf} in Eq. (12). Using Eq. (2), the void spacing ratio at coalescence λ_c follows as

$$\lambda_c = \frac{2\chi_c^3}{3f_{Vc}^{cell}}. \quad (55)$$

Moreover, λ_c can be estimated as a function of ε_{mc} following Eq. (19) as

$$\ln \frac{\lambda_c}{\lambda_0} = \kappa \varepsilon_{mc}^{cell}. \quad (56)$$

Since both $\ln \frac{\lambda_c}{\lambda_0}$ and ε_{mc}^{cell} are known, the value of κ is given by linear regression. The value $\kappa = 1.22$ is found as shown in Fig. 4b from the unit cell simulations and when considering the values of q_1 , q_2 calibrated here before.

Using the calibrated values of $q_1 = 1.414$, $q_2 = 1$, and $\kappa = 1.22$, the solutions of both the GTN model and the GTN/Thomason model can be reproduced and compared with the ones obtained with the unit cell simulations. The results are shown in Fig. 5. A good agreement between the GTN/Thomason model and the unit cell simulations is observed as needed to safely proceed with the full model.

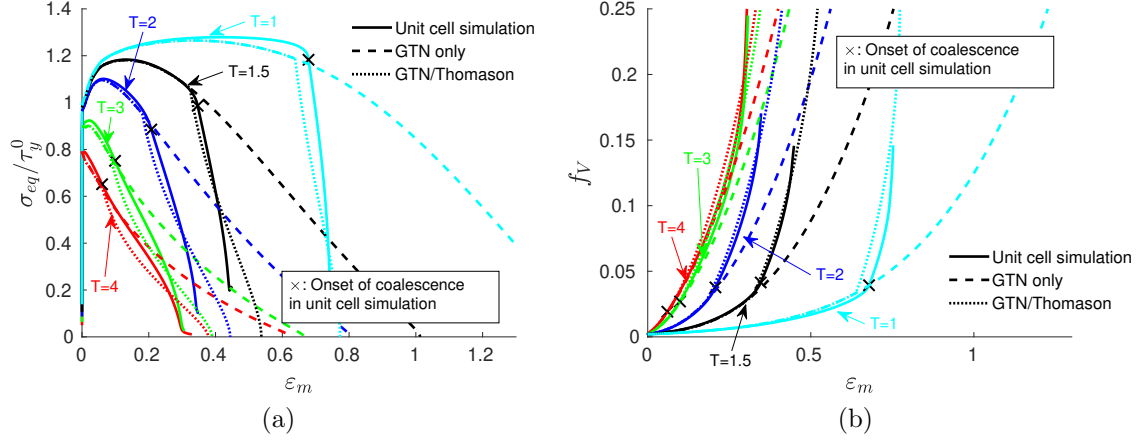


Figure 5: Comparison between the results obtained with unit cell simulations, the GTN model only, and the coupled GTN/Thomason model at different stress triaxiality values: (a) σ_{eq} in terms of ϵ_m and (b) f_V in terms of ϵ_m . The points at which the results obtained with the GTN/Thomason model deviate from the ones obtained with the GTN model correspond to the onset of coalescence in the GTN/Thomason model.

3.2. Identification of l and h_b

The nonlocal length l controls the dissipated energy during the void evolution through the nonlocal diffusion Eq. (13). The value of l should scale or be commensurable with the inter-distance of the relevant heterogeneities [67], *i.e.* the inter-void spacing in the current context. For the material under consideration, the inter-void spacing is almost similar in the longitudinal and transverse directions and approximately equal to $100 \mu\text{m}$. As a result, the length $l = 100 \mu\text{m}$ is selected for the subsequent analyses to see if a physically motivated choice is appropriate in the context of the present nonlocal formulation.

The cohesive band thickness h_b should be representative also of the mechanisms at play. Scheyvaerts et al. [24] have analyzed in details the void geometry at, and, during coalescence. Since the plastic flow during coalescence localizes inside the ligament between voids, the characteristic length can be related to the void size. As a matter of fact, the band thickness can be either smaller or larger than the diameter of the voids. From the microstructural analysis, this average radius of MnS inclusions along the longitudinal axis is approximately equal to $8 \mu\text{m}$. Therefore, the cohesive band thickness $h_b = 8 \mu\text{m}$ is taken. However, this first choice will have to be validated either by cell simulations or by mechanical tests performed on controlled crack propagation specimens as the compact test specimens, as it will be done in Section 6, or as the double edge notched specimens. One can obtain a more accurate estimate for the coalescence characteristic size by evaluating the relative thickness inside which the plastic flow localizes during the unit cell simulations. Alternatively, the fitting between the numerical and the experimental dissipated energies allows the h_b values to be estimated. Moreover, an anisotropy effect is likely to appear because of the fracture anisotropy extracted along different orientations.

3.3. Identification of k_ω

The last remaining parameter, the shear-induced void growth factor k_ω of the nonlocal GTN-NH/Thomason model, is calibrated by fitting the fracture strain predicted by the GTN-

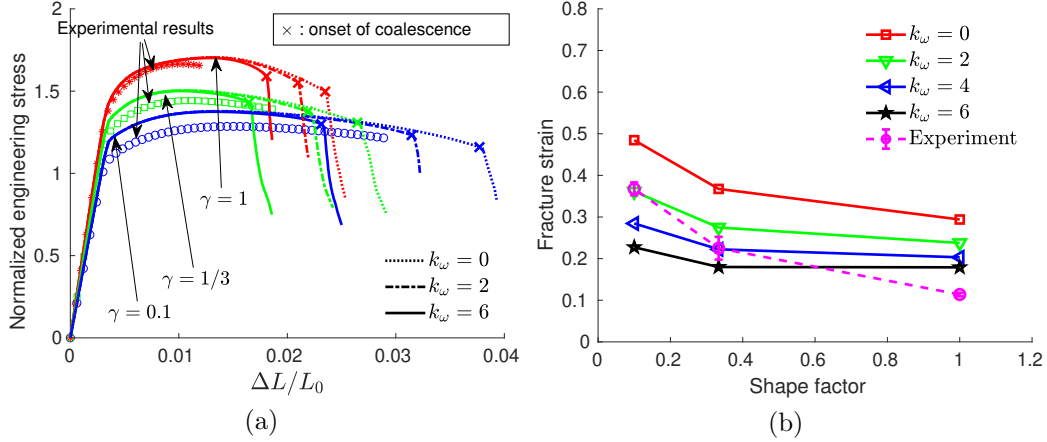


Figure 6: Influence of k_w in the response of the plane strain specimens: (a) normalized engineering stress in terms of the engineering strain and (b) fracture strain and corresponding experimental measurements. The experimental curves correspond to average responses obtained for different specimens with the same geometry and are truncated once one of the specimen responses exhibits a sudden drop.

NH/Thomason model with the ones measured from the experimental tests performed on the plane strain (PE) specimens, see the full description provided in the next Section. These experimental results are preferred among all the available tests because of their underlying stress state, in which the Lode parameter ζ is equal to 0 at the center of the specimen. This stress state maximizes the effect of k_w on the void evolution following Eq. (17).

The numerical simulations model only the central part of the plane strain specimens within the gauge length L_0 . The finite element meshes are similar to the elastoplastic simulations performed in Part I [1]. The presence of the notch is characterized by the shape factor, denoted by γ , which is defined as the ratio between the half thickness at the notch section ($\frac{t_0}{2}$ with t_0 being the initial thickness at notch) and the notch radius (denoted by R_n), *i.e.*

$$\gamma = \frac{t_0}{2R_n}. \quad (57)$$

The numerical simulations are performed with $\gamma = 0.1, 1/3$, and 1. The value of k_w is varied from 0 to 6.

The evolution of the engineering stress as a function of the engineering strain is shown in Fig. 6a. The onset of coalescence for each case is also reported with a fast stress drop observed after this point. As expected, a larger value of k_w enhances the porosity growth rate, leading to an earlier onset of coalescence. For each case of given γ and k_w , the fracture strain is estimated in a similar way as in the experimental tests with

$$\bar{\epsilon}_f = \frac{2}{\sqrt{3}} \ln \frac{t_0}{t_c}, \quad (58)$$

where t_c is the specimen thickness measured at its center, at the occurrence of the onset of coalescence. The corresponding fracture strains of all the numerical simulations are summarized in Fig. 6b. The experimental values obtained in Part I [1] are also reported. Increasing

k_ω decreases the value of $\bar{\epsilon}_f$. However, a smaller effect for a smaller notch radius (higher γ) is observed as the stress triaxiality is higher in that specimen. Using a rule of thumb to choose a value between $k_\omega = 4$ and $k_\omega = 6$, the value of $k_\omega = 5$ is chosen. The numerical predictions with $k_\omega = 5$ are reported in Section 4.3.

4. Validation of the nonlocal GTN-NH/Thomason model

All the material parameters required for the nonlocal coupled GTN-NH/Thomason model summarized in Tab. 1 were identified above or in Part I, see Tab. 2. In the following, the GTN-NH/Thomason model with the identified parameters is used to simulate the experimental tests. The simulations are performed without the damage-to-crack transition formalism.

Table 2: Porous plastic parameters of the nonlocal GTN-NH/Thomason model.

| q_1 | q_2 | α | β | l | f_{V0} | λ_0 | k_ω | κ |
|-------|-------|----------|---------|-------------------|----------|-------------|------------|----------|
| 1.414 | 1 | 0.129 | 1.24 | 100 μm | 0 | 1 | 5 | 1.22 |

4.1. Summary of the specimen geometries

For the ease of readability, the specimen geometries considered in the experimental campaign performed in Part I are reminded. Three different geometry types were tested including round bars (denominated by RB) specimens, plane strain (denominated by PE) specimens, and plane stress (denominated by PS) specimens, see Fig. 7. The presence of a notch in the specimens (including RB, PE, and PS types) is characterized by the shape factor, denoted by γ and given by

$$\gamma = \frac{a_0}{R_n}, \quad (59)$$

where R_n is the notch radius and a_0 is defined based on the specimen type: (i) for RB, $a_0 = R_0$ where R_0 is the initial radius at the notch section, (ii) for PE, $a_0 = t_0/2$ where t_0 is the initial in-plane thickness at notch section, see also Eq. (57), and (iii) for PS, $a_0 = W_0/2$ where W_0 is the initial width at the notch section. For smooth specimens, $\gamma = 0$ since $R_n \rightarrow \infty$. In order to assess the influence of material anisotropy, the RB specimens are extracted in both the longitudinal direction (notation prefixed by L) and the transverse direction (notation prefixed by T). Since the other specimens are extracted following the longitudinal direction only, the prefix L- is omitted for conciseness. The specimen names and corresponding shape factors are summarized in Tab. 3.

The RB specimens are modeled with axisymmetric finite elements using 6-node triangular elements. Plane strain 6-node triangular elements are used to model the PE specimens. The PS specimens need 3-dimensional finite element simulations in which 10-node tetrahedral elements are used. All the meshes are refined within the necking region with at least 2 elements covering the nonlocal length in order to capture the large local stress and strain gradients. Moreover, mesh size sensitivity analyses were systematically performed to ensure a sufficient refinement and to present converged results of the fracture strain. As a result, the finite element meshes are the same as the one used in the elastoplastic analysis performed in

Part I. The numerical integration is performed using an implicit time integration so that the inertial forces can stabilize the local snapbacks that could possibly occur, in particular when introducing the cracks in the next section.

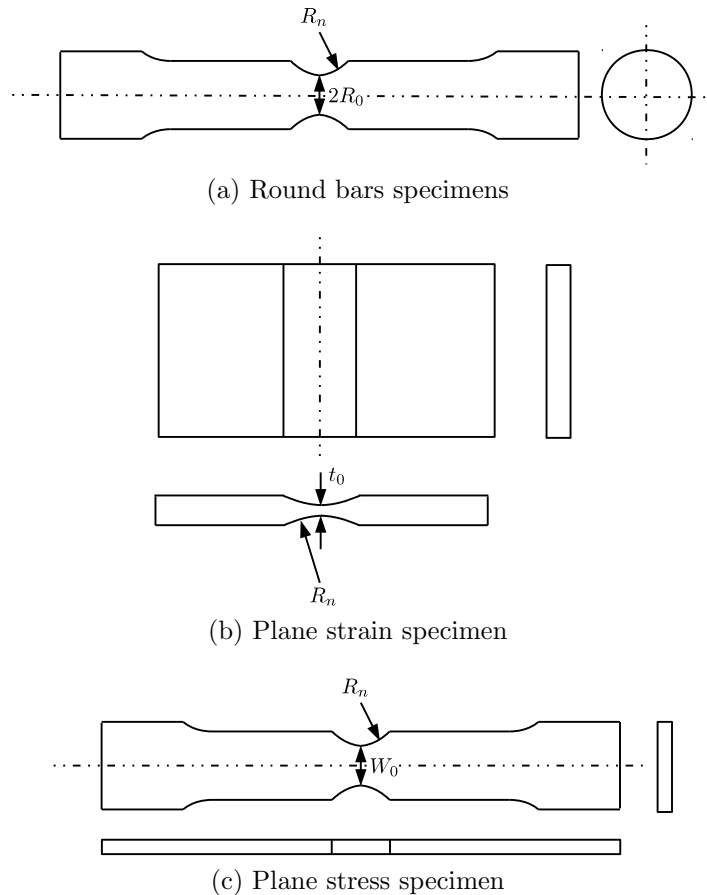


Figure 7: Sample geometries used in this study consist of (a) round bar (RB) specimens with $R_0 = 3$ mm, (b) plane strain (PE) specimens with $t_0 = 2$ mm, and (c) plane stress (PS) specimens with $W_0 = 7$ mm and thickness equal to 2 mm.

4.2. Tensile tests on the RB specimens

Figures 8a and 8b show the comparison for the RB specimens between the results of the GTN-NH/Thomason model and the experimental results. The result of the elastoplastic simulation for the SRB specimens is also reported in Fig. 8a. After the onset of coalescence, with the GTN-NH/Thomason model, the force drops until almost zero, signifying full specimen fracture. The fracture strain can then be approximately evaluated at that time as

$$\bar{\epsilon}_f = 2 \ln \frac{R_0}{R_c}, \quad (60)$$

where R_c is the notch radius when the onset of coalescence occurs at the specimen center. The predicted fracture strains of the RB specimens are compared in Fig. 8c to the experimental data. A good agreement is obtained within 20 % relative error maximum for almost all

Table 3: Sample names with the corresponding shape factor [1].

| Type | Test case | Extracted direction | Shape factor γ |
|----------------------|-----------|---------------------|-----------------------|
| Smooth Round Bar | SRB | L, T | 0 |
| Notched Round Bar | NRB-1 | L, T | 0.75 |
| Notched Round Bar | NRB-2 | L, T | 1.5 |
| Notched Round Bar | NRB-3 | L, T | 2 |
| Notched Round Bar | NRB-4 | L | 3 |
| Notched Plane Strain | NPE-1 | L | 0.1 |
| Notched Plane Strain | NPE-2 | L | 0.33 |
| Notched Plane Strain | NPE-3 | L | 1 |
| Smooth Plane Stress | SPS | L | 0 |
| Notched Plane Stress | NPS-1 | L | 0.75 |
| Notched Plane Stress | NPS-2 | L | 1.5 |
| Notched Plane Stress | NPS-3 | L | 2.9 |

cases (except for the T-SRB and T-NRB-3 specimens that exhibit a higher relative error respectively equal to 26% and 35%). The capability of the anisotropic nucleation model in capturing the anisotropic fracture behavior is demonstrated with a higher predicted fracture strain in the longitudinal specimens.

For the case of the L-RB specimens reported in Fig. 8c, when increasing the shape factor γ , the fracture strain first decreases before stabilizing and exhibiting even a slight increase for values of γ in the range [2 4]. For larger values of γ , the fracture strain decreases again. This trend of the fracture strain results from the competition between the plastic flow and the stress triaxiality effects, whose distributions depend on the shape factor of the specimen. The impact of the plastic deformation at the free surface of the notched section becomes dominant on setting the magnitude of the fracture strain for increasing values of γ . At low values of γ ($\gamma \leq 2$), the center of the specimen is subjected to a higher stress triaxiality state and lower plastic deformation, while the free surface of the notched section involves a lower stress triaxiality and a higher plastic deformation. As a result, the initiation of the void coalescence process occurs at the center of the specimen for values of $\gamma \leq 2$. In the intermediate range, $2 < \gamma \leq 4$, the void coalescence still initiates at the center of the specimen, but the plastic flow at the free surface of the notched section becomes more intense, leading to a slight increase of the observed fracture strain due to the globally more important plastic deformations at coalescence onset at the specimen center. It is noted that Eq. (60) is also used to estimate the fracture strain in the experimental tests for the RB specimens as shown in Part I. When the value of γ is large enough ($\gamma \geq 4$), because of the increase of the plastic flow at the free surface, the location of the initiation of void coalescence moves to the free surface of the notched section. In a limit case when $\gamma \rightarrow \infty$, a crack initiates at the free surface and the plastic deformation localizes at the crack front where coalescence occurs. Although such a range of γ is not considered, the experimental fracture strains for the L-RB specimens with $\gamma = 2$ and $\gamma = 3$ also exhibit a slight increase after the considerable decrease observed for $\gamma \leq 2$ as shown in Fig. 8c.

The distributions along a transverse middle cross section of several internal variables

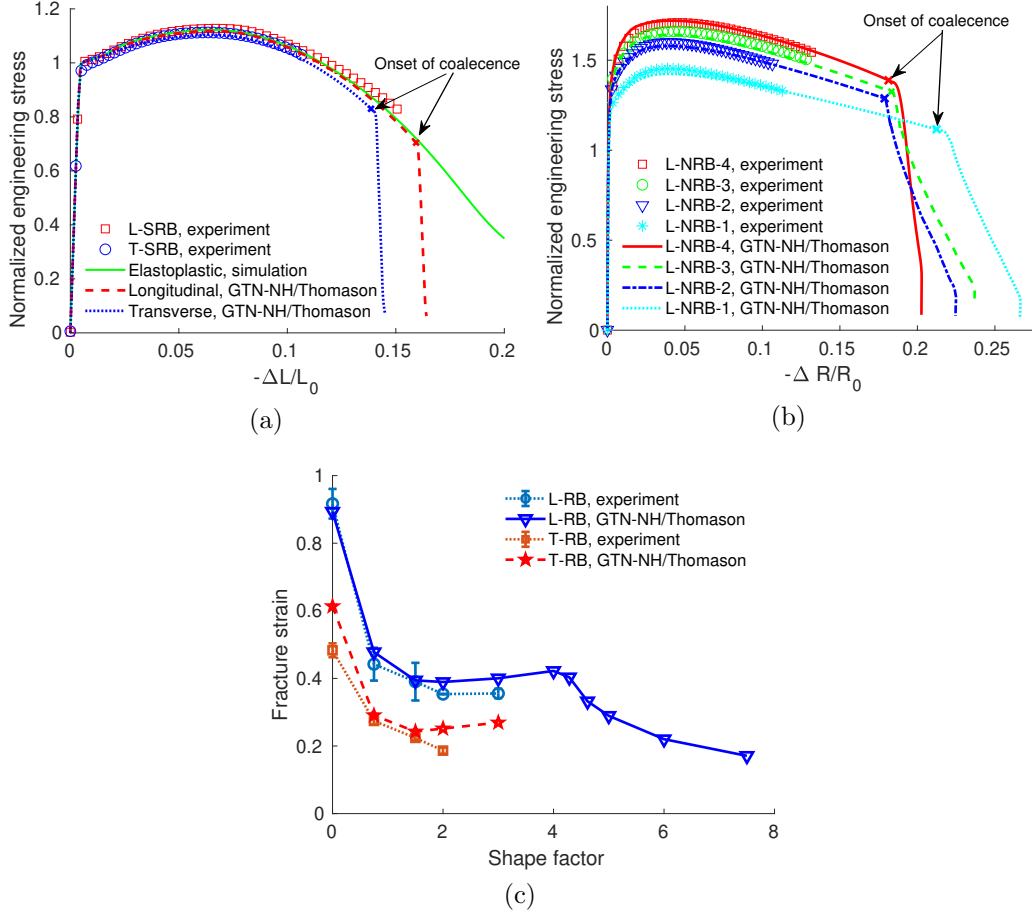


Figure 8: RB specimens simulated with the nonlocal coupled GTN-NH/Thomason model: (a) normalized engineering stress in terms of the engineering strain in the case of the SRB specimens, (b) normalized engineering stress in terms of the engineering strain in the case of the NRB specimens, and (c) fracture strain for all the RB specimens. The experimental curves correspond to average responses obtained for different specimens with the same geometry and are truncated once one of the specimen responses exhibits a sudden drop.

in the cases of the SRB specimens are compared for both specimen orientations in Fig. 9 at the onset of coalescence and in Fig. 10 at the final fracture stage. The plastic strain values ε_m are higher in the longitudinal specimen compared to the transverse one due to the higher ductility while the effective nonlocal porosity⁴ value \tilde{f}_V is higher for the latter. Comparable values are observed for the ligament ratio χ at the onset of coalescence showing that this parameter is the one controlling coalescence. Besides, beyond the initiation of void coalescence, the simulations produce a flat fracture path for both specimen orientations, see Fig. 10. The predicted fracture path does not agree with the experimental observations, in which cup-cone fracture paths were observed. Indeed the current GTN-NH/Thomason model

⁴The GTN-NH model considers the effective porosity which characterizes effective spherical voids and is different from the apparent porosity by a factor related to the void aspect ratio as explained in Part I.

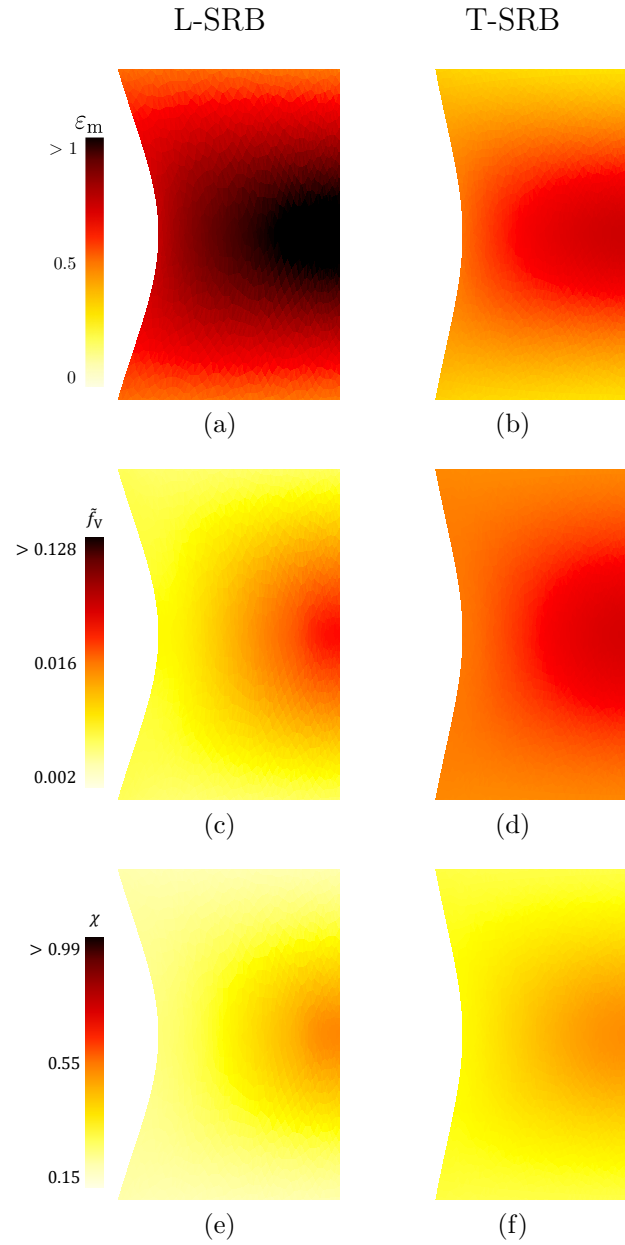


Figure 9: SRB specimens simulated with the nonlocal coupled GTN-NH/Thomason model: distributions of (a-b) the matrix plastic strain ε_m , (c-d) the nonlocal porosity \tilde{f}_V , and (e-f) the ligament ratio χ in the deformed configuration at the onset of coalescence for specimens cut in the longitudinal direction (left) and in the transverse direction (right).

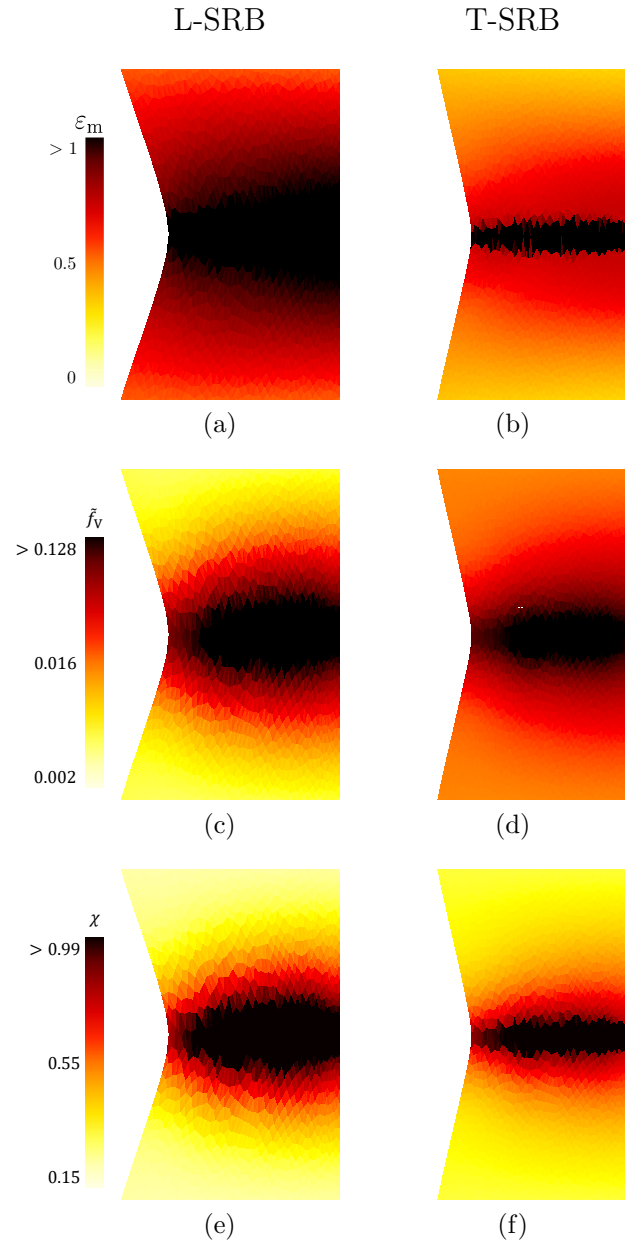


Figure 10: SRB specimens simulated with the nonlocal coupled GTN-NH/Thomason model: distributions of (a-b) the matrix plastic strain ε_m , (c-d) the nonlocal porosity \tilde{f}_V , and (e-f) the ligament ratio χ in the deformed configuration at final fracture for specimens cut in the longitudinal direction (left) and in the transverse direction (right).

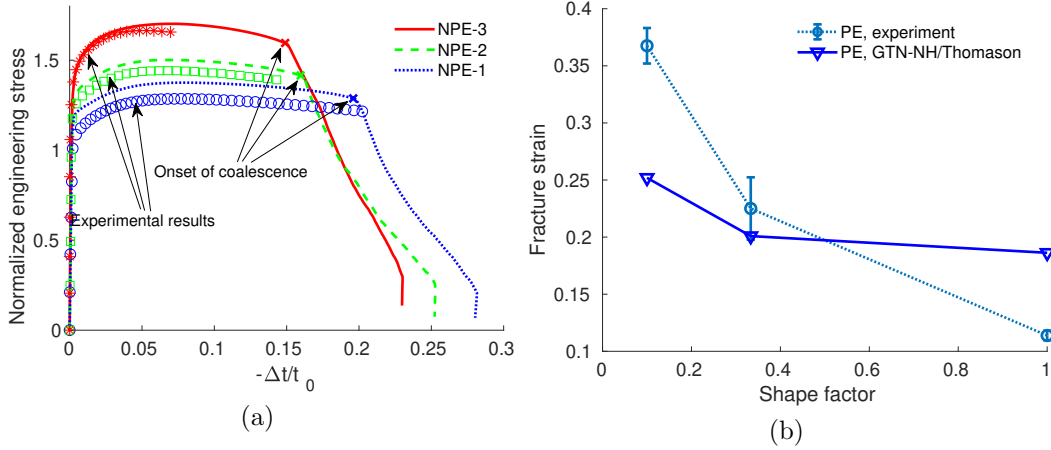


Figure 11: PE specimens simulated with the nonlocal coupled GTN-NH/Thomason model: (a) normalized engineering stress in terms of the engineering striction and (b) fracture strain. The experimental curves correspond to average responses obtained for different specimens with the same geometry and are truncated once one of the specimen responses exhibits a sudden drop.

does not include the possibility for a shear coalescence mode. The cup-cone fracture paths will come naturally using the damage-to-crack transition framework [39] as shown later.

4.3. Tensile tests on the PE specimens

Figure 11a shows the overall response of the PE specimens in terms of the force versus thickness reduction at the notch section. A smaller notch radius results in a higher stress level and earlier cracking initiation. The onset of coalescence at the specimen center is also marked. After this point, material softening is visible due to the propagation of the void coalescence. The values obtained for all the PE specimens are shown in Fig. 11b compared to the experimental measurements. The numerical predictions underestimate the experimental results for $\gamma = 0.1$ and $1/3$ while the experimental result is overestimated for $\gamma = 1$.

The distributions of some representative internal variables are shown in Fig. 12 at the onset of coalescence and in Fig. 13 near the last fracture stage. Although inclined plastic bands develop at the onset of the coalescence, flat crack paths are predicted during the post-coalescence stage. This erroneous fracture path arises because the Gurson-Thomason model does not include the shear coalescence mode as explained above for the SRB specimen. However, the slant path will be captured with the damage-to-crack transition framework as shown in Section 5.

The sets of simulation results for both the RB and PE specimens do not present an extended artificial diffusion of damage as it can be observed for some nonlocal damage model, see respectively Figs. 9, 10 and Figs. 12, 13. Indeed, considering a pure GTN-NH model, since the porosity which controls the damage evolution is considered as the nonlocal variable, such a artificial spread could be expected and could be avoided by decreasing the nonlocal length [67, 68], but the yield surface acts as filter limiting this phenomenon. Besides, in the considered case of the GTN-NH/Thomason model, the Thomason coalescence yield function (11) shrinks fast and much faster than the GTN-NH one, allowing for the elastic unloading,

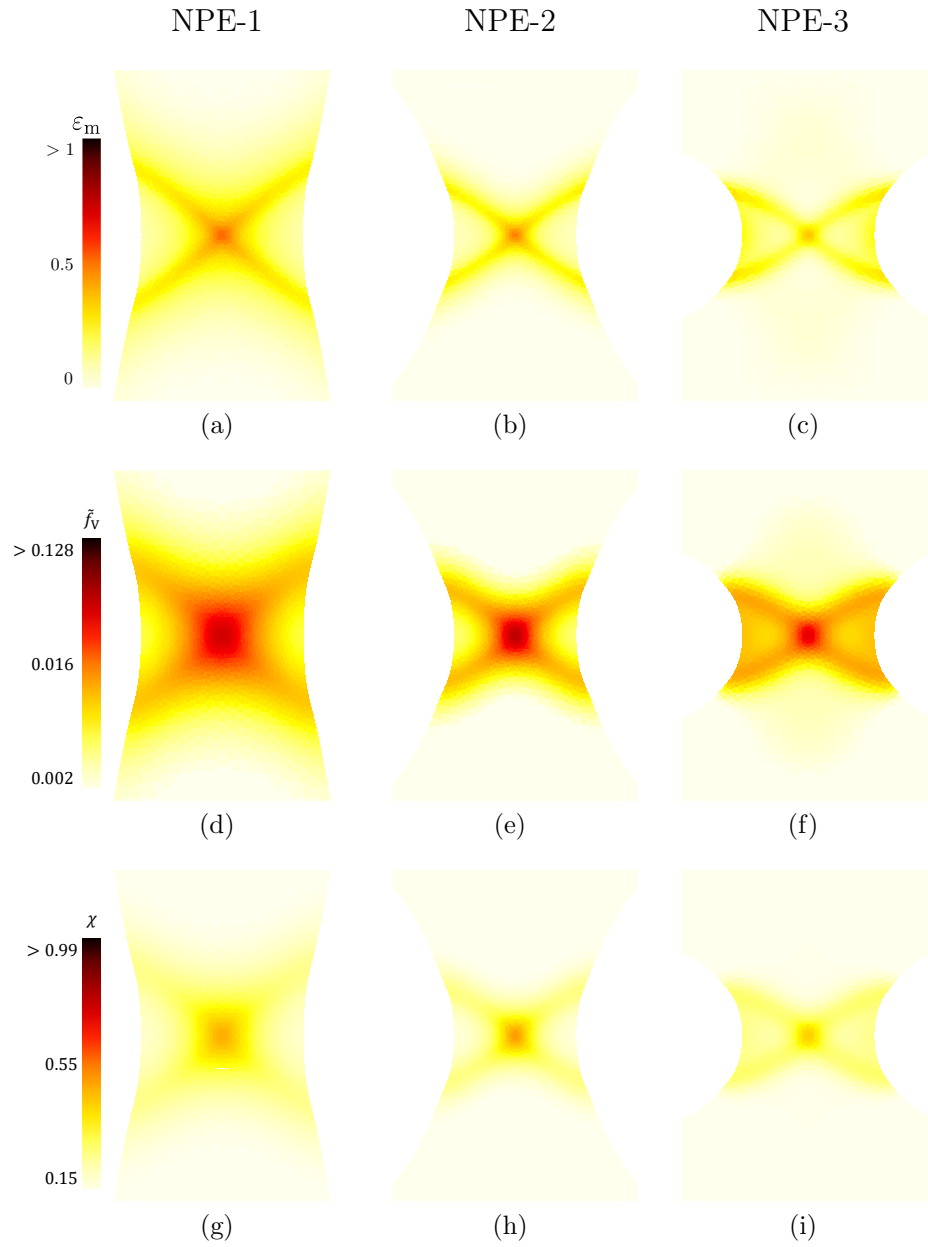


Figure 12: PE specimens simulated with the nonlocal coupled GTN-NH/Thomason model: distributions of (a-c) the matrix plastic strain ε_m , (d-f) the nonlocal porosity \tilde{f}_V , and (g-i) the ligament ratio χ in the deformed configuration at the onset of coalescence.

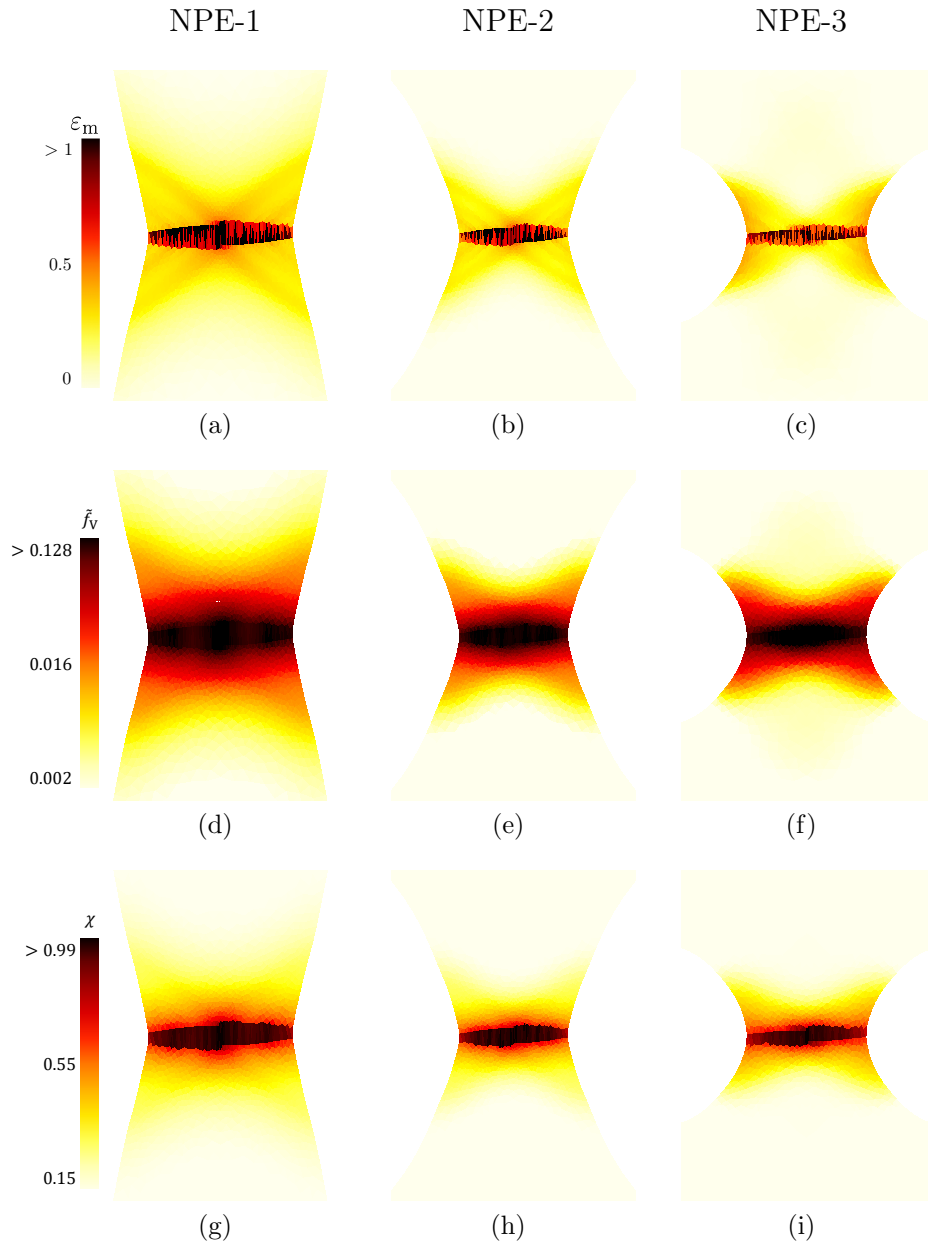


Figure 13: PE specimens simulated with the nonlocal coupled GTN-NH/Thomason model: distributions of (a-c) the matrix plastic strain ε_m , (d-f) the nonlocal porosity \tilde{f}_V , and (g-i) the ligament ratio χ in the deformed configuration near last fracture stage.

which is governed by the GTN-NH model, outside of the localization band to occur despite the fact that the nonlocal porosity spreads. We can observe for the PE specimens, see Fig. 13, that the ligament ratio χ localizes in a single-element thick band. Finally, the introduction of the crack in the next section will totally prevent the artificial diffusion of the porosity and will circumvent the issue of ligament ratio localization in a single-element thick band.

4.4. Tensile tests on the PS specimens

As only the fracture strain is of interest, the simulations of the PS specimens are interrupted at the onset of coalescence. The evolution of the applied force in terms of the reduction of the notch section is shown in Fig. 14a. Based on the rough assumption that the minimum cross-section at failure remains rectangular, the fracture strain for this geometry can be approximated by

$$\bar{\epsilon}_f = \frac{2}{\sqrt{3}} \sqrt{\ln^2 \frac{W_0}{W_f} + \ln^2 \frac{t_0}{t_f} + \ln \frac{W_0}{W_f} \ln \frac{t_0}{t_f}}, \quad (61)$$

where W_0 and W_f are respectively the initial specimen width at the notch and the width at failure, and where t_0 and t_f are respectively the initial thickness at the notch and the thickness at failure. It is noted that Eq. (61) is also used to estimate the fracture strain in the experimental test specimens as shown in Part I. The numerical fracture strains are estimated at the onset of coalescence in the specimen center and are reported in Fig. 14b where they are compared to the experimental measurements, showing a good agreement as well.

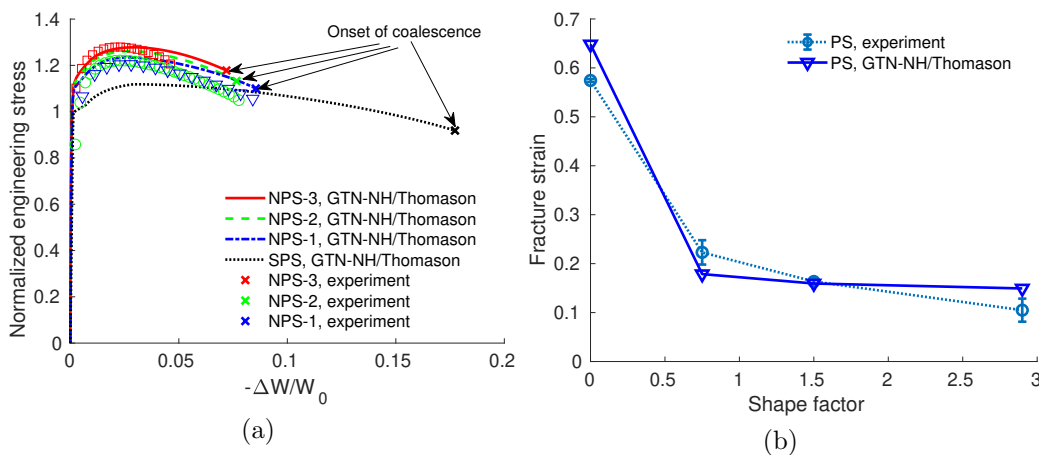


Figure 14: PS specimens simulated with the nonlocal coupled GTN-NH/Thomason model: (a) normalized engineering stress in terms of the engineering striction and (b) fracture strain. The experimental curve of the SPS specimen is not available. The experimental curves correspond to average responses obtained for different specimens with the same geometry and are truncated once one of the specimen responses exhibits a sudden drop.

4.5. Summary of the fracture strains for all specimens

The fracture strain data for all specimens reported in Figs. 8c, 11b and 14b are summarized in Fig. 15 in terms of the stress triaxiality and Lode parameter. For the RB and PE specimens, as the Lode parameter remains constant, the fracture strain decreases with increasing stress triaxiality, see Fig. 15a. Although the range of the stress triaxiality in these specimens is similar, the fracture strains differ since the values of the Lode parameter are different. For the PS specimens, both the stress triaxiality and the Lode parameter vary with the notch radius and the fracture strain increases as the Lode increases as already discussed in Part I, see Fig. 15b. As shown in Fig. 15b, the Lode parameter can be smaller than 0.2 for some PS specimen geometries, in which case the effect of k_ω in the void growth expression (17) is significant, which validates the choice of $k_\omega = 5$. Besides, the choice of the nonlocal length scale which was physically motivated according to the microstructure characterization as discussed in Section 3.2, leads to numerical predictions of the fracture strain in reasonable agreement with the experimental measurements, which confirms the selection of such a physically motivated length scale parameter for the considered microstructure.

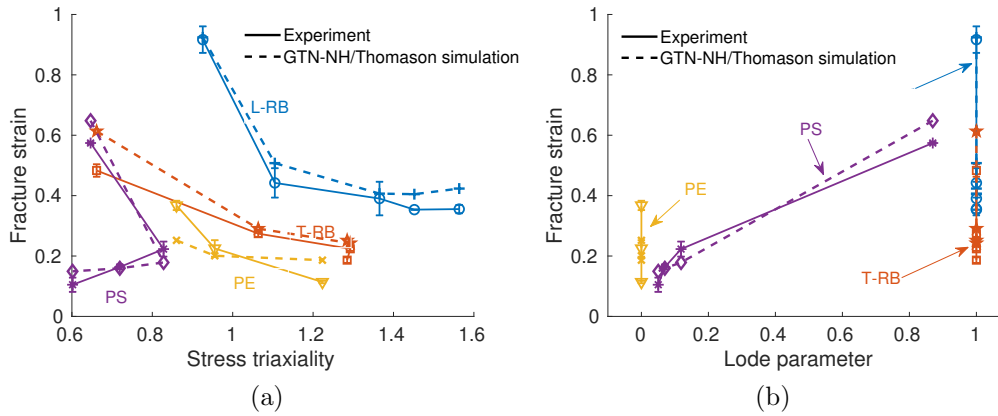


Figure 15: Comparison between the fracture strain predicted by the GTN-NH/Thomason model and the corresponding experimental results in terms of the true stress state at the onset of fracture: (a) dependence on the stress triaxiality and (b) dependence on the Lode parameter.

5. Validation of the damage-to-crack transition

The nonlocal coupled GTN-NH/Thomason formalism is now enriched by the damage-to-crack transition framework presented in Section 2.2 in order to assess the capability of this framework to recover the experimentally observed crack paths. Comparatively to the simulations of the previous sections, a scatter of 1% is applied on the nucleation intensity to promote crack kinking as it is often the case for fracture simulations involving cohesive models. The combination of the creation of the free surfaces due to the damage-to-crack transition with this scatter, which introduces imperfections in the model to avoid the crack path to be artificially guided by the mesh regularities, promotes crack kinking [39].

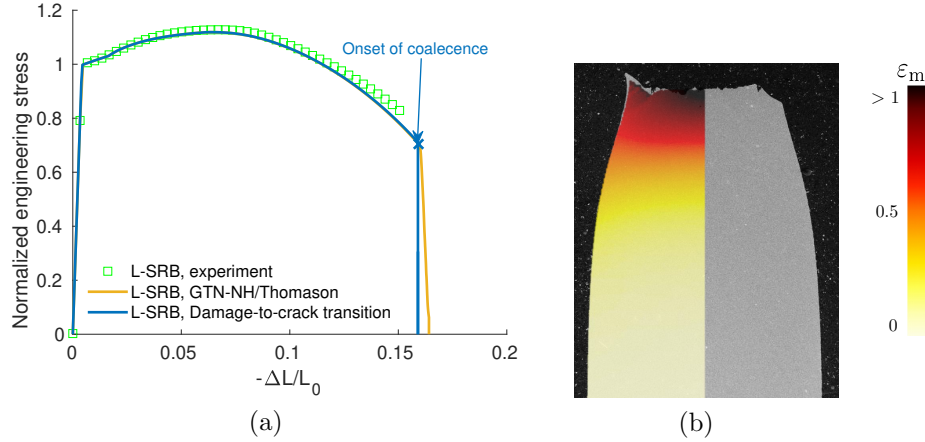


Figure 16: Damage-to-crack transition for the L-SRB specimen: (a) comparison of the normalized engineering stress in terms of the engineering strain, in which the numerical results provided with the nonlocal GTN-NH/Thomason model, with and without the damage-to-crack transition, and the experimental result are reported, and (b) comparison of the cup-cone failure pattern obtained with the numerical simulation and with the experimental test.

5.1. Tensile test on the L-SRB specimen

The deformation of the L-SRB specimen has been simulated using the damage-to-crack transition framework. The numerical simulation requires about 1000 increments for a total of 32 hours computational time on a single processor, to be compared with 2h30 of computational time for the nonlocal GTN-NH/Thomason model. The force evolution as a function of the engineering strain is represented in Fig. 16a for the nonlocal model with and without using a crack insertion mechanism. Before crack insertion, no difference is found as only the nonlocal GTN-NH is activated. After crack insertion, the differences are significant as the local form of the Thomason model governs the crack opening. The drop of the load carrying capacity is steeper with the transition.

The distributions of the matrix plastic strain ϵ_m , the nonlocal porosity \tilde{f}_V and the ligament ratio χ are illustrated in Fig. 17 in the deformed configuration at different stages of the failure process: at the onset of coalescence, before the bifurcation of the crack into a slant mode, and at final fracture. Before crack insertion, the results are identical to the nonlocal model, see Fig. 9. A crack then initiates at the center of the specimen and propagates radially, following the elements boundary. At some point, near the free surface, shear bands appear ahead of the crack front and the crack kinks at around 45° to propagate until it reaches the surface. This results in the so-called cup-cone fracture, typically observed in the literature [4] for different types of tensile test specimens. The fracture pattern predicted by the numerical method is found to be in good agreement with the experimental broken specimen as illustrated in Fig. 16b.

5.2. Tensile test on the NPE-1 specimen

The damage-to-crack transition is now applied for a different stress state on the NPE-1 specimen. The numerical simulation requires about 3200 increments for a total computational time of 15 hours on a single processor. The evolution of the applied force is shown in Fig. 18.

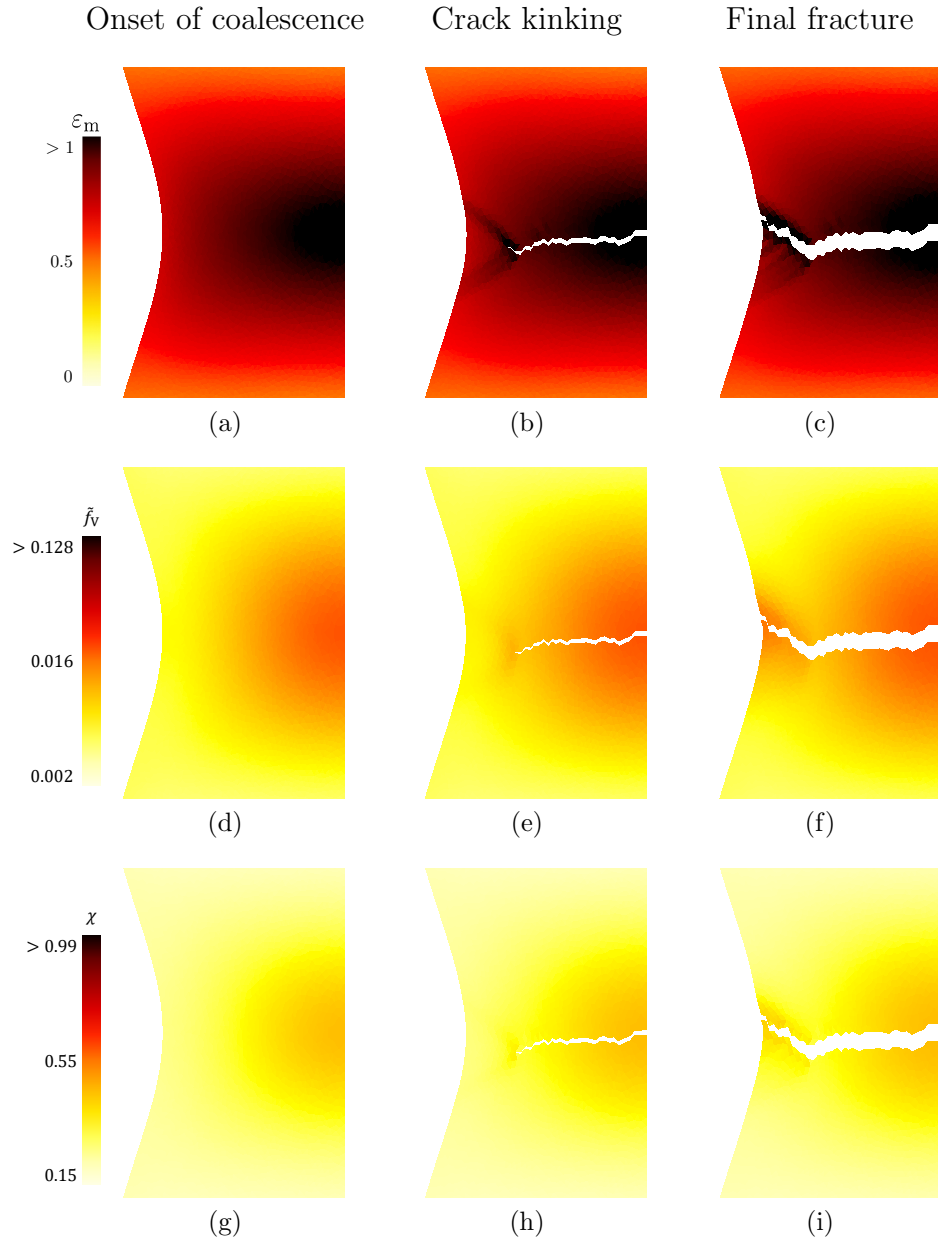


Figure 17: Distributions predicted by the nonlocal GTN-NH/Thomason model with the damage-to-crack transition of (a-c) the matrix plastic strain ε_m , (d-f) the nonlocal porosity \tilde{f}_V , and (g-i) the ligament ratio χ in the deformed configuration for the L-SRB specimen at different stages: (left) at the onset of coalescence, (center) before crack kinking and (right) at final fracture.

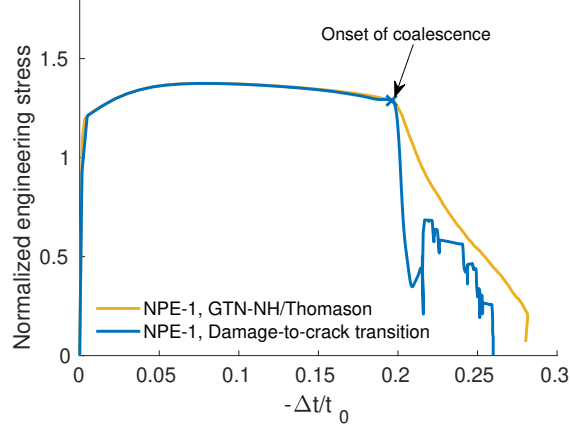


Figure 18: Comparison of the normalized engineering stress in terms of the engineering striction with the NPE-1 specimen. The numerical results are provided with the nonlocal GTN-NH/Thomason model with and without the damage-to-crack transition.

Oscillations are also visible. They are due to the propagation of stress waves resulting from the dynamic integration scheme and from the lower dissipation associated to the transition resulting from the total absence of spurious damage diffusion. The damage dissipation is more limited after crack initiation than without the crack insertion formalism. The distributions of the matrix plastic strain ε_m , the nonlocal porosity \tilde{f}_V and the ligament ratio χ in the deformed configuration are shown on Fig. 19. By opposition to the previous case, the plastic strain localizes inside shear bands. The crack also initiates at the center and then propagates towards the surface, forming a slant crack. Comparatively to the smooth round bar, fracture occurs at a lower level of plastic strain while the porosity is higher. This observation is due to a higher triaxiality level compared to the smooth round bars, amplified by a contribution in shear. A slant crack is observed on the numerical simulations, coherently to the experimental observation, see Part I [1], providing another validation of the predictive character of the model.

6. Application to a stable crack propagation: compact tension specimen

In this section, the case of stable propagation is studied both numerically and experimentally on a compact test (CT) specimen in order to validate the model characteristic lengths, *i.e.* the non-local length controlling the GTN-NH/Thomason model and the cohesive band thickness governing the crack opening once inserted upon coalescence onset.

The geometry and the extraction direction of the specimens are reported in Fig. 20. The extraction direction of the specimens results in a crack opening under the transverse direction of the material. An initial fatigue crack was obtained by cyclic loading. Three different specimens were tested. The reaction force F at the loading spurs *vs.* the crack mouth opening Δ was recorded as sketched in Fig. 20a. The crack was observed to propagate straight ahead in all the experimental tests.

The finite element simulations are performed with the damage-to-crack transition under two-dimensional plane strain condition. Four different finite element meshes with different mesh sizes are considered to assess the mesh influence: Mesh 1 (the coarsest), Mesh 2, Mesh

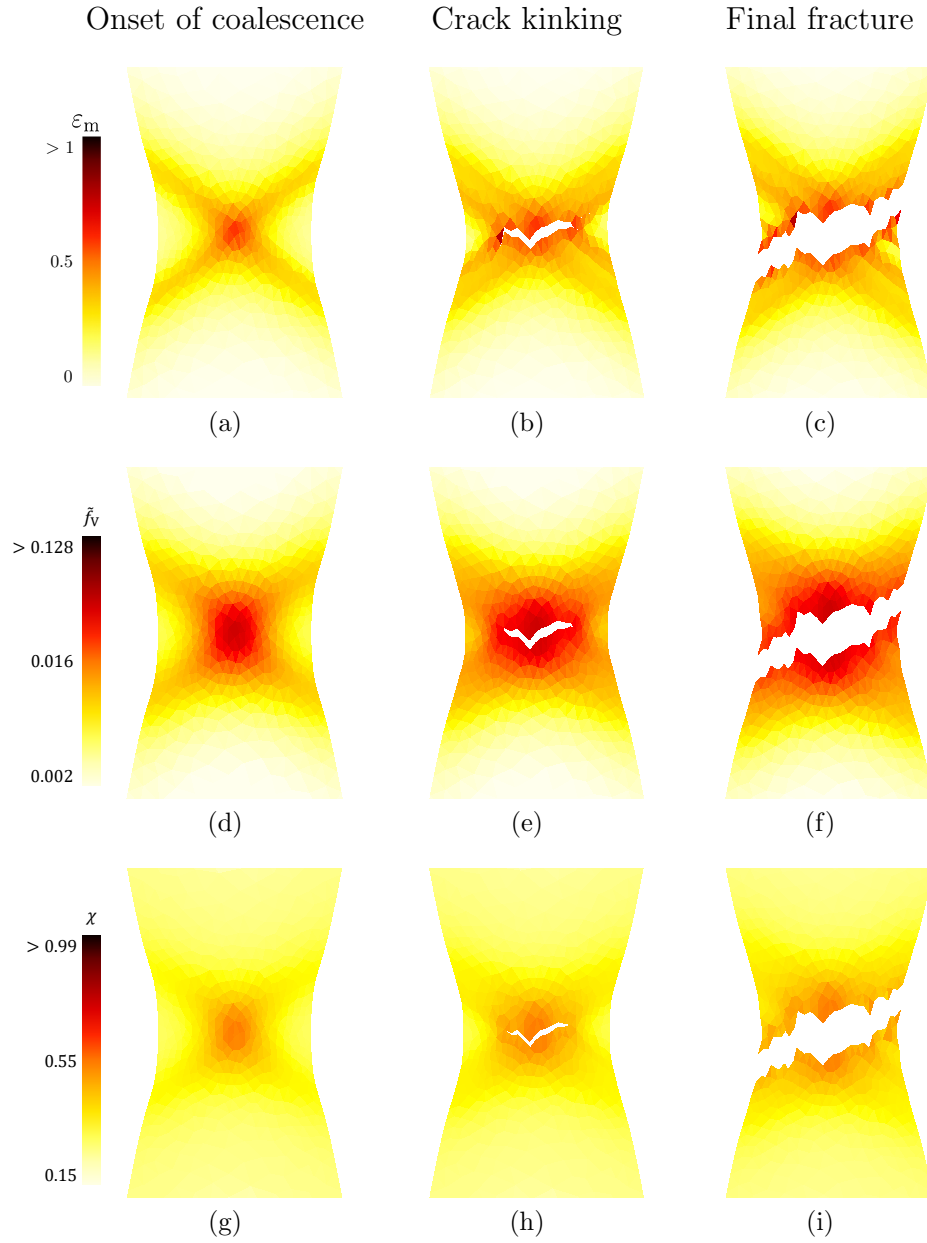


Figure 19: Distributions predicted by the nonlocal GTN-NH/Thomason model with the damage-to-crack transition of (a-c) the matrix plastic strain ε_m , (d-f) the nonlocal porosity \tilde{f}_V , and (g-i) the ligament ratio χ in the deformed configuration for the NPE-1 specimen at different stages: (left) at the onset of coalescence, (center) before crack kinking and (right) at final fracture.

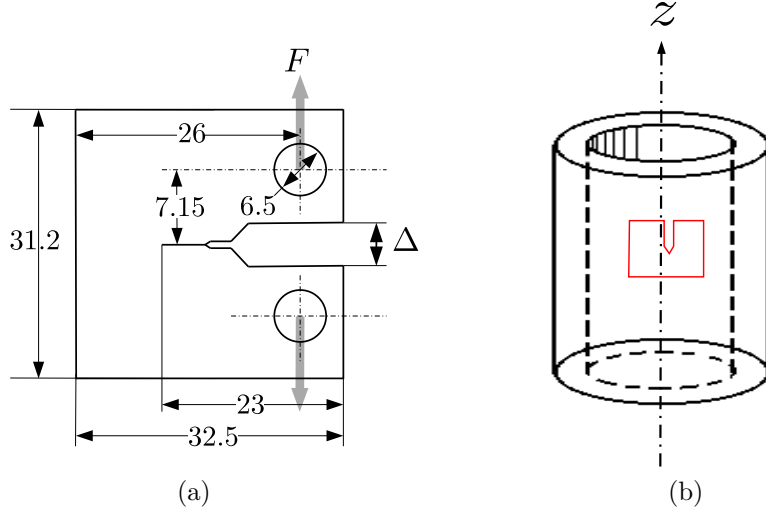


Figure 20: Compact test (CT) specimen: (a) geometry in mm and (b) extraction direction of the specimen from the hollow cylindrical piece. The thickness of the CT specimen is equal to 13 mm. The reaction force F vs. the crack mouth opening Δ is recorded during the experimental tests.

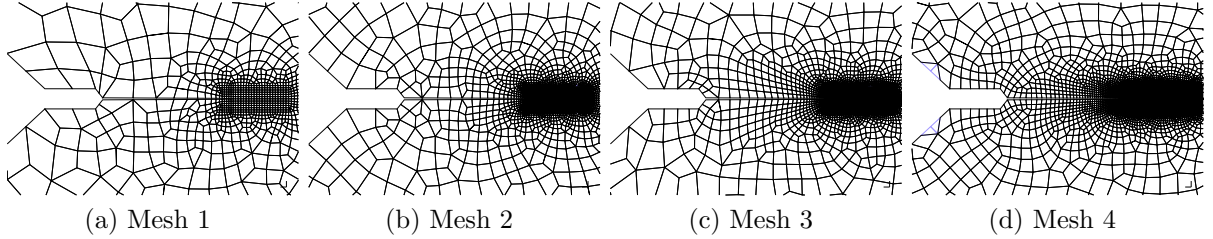


Figure 21: Mesh discretizations of the compact test (CT) specimen: (a) Mesh 1 with element size of $60 \mu\text{m}$ at fatigue crack tip, (b) Mesh 2 with element size of $30 \mu\text{m}$ at fatigue crack tip, (c) Mesh 3 with element size of $20 \mu\text{m}$ at fatigue crack tip, and (d) Mesh 4 with element size of $10 \mu\text{m}$ at fatigue crack tip.

3, and Mesh 4 (the finest), respectively consisting of 1800, 3270, 5200, and 13860 quadratic quadrangles, see Fig. 21. Since the crack is propagating straight ahead, quadrangle meshes are used for simplicity.

The comparison between the numerical and the experimental results in terms of the normalized reaction force vs. crack opening is reported in Fig. 22. The peak of the curve requires a very fine mesh to be captured since the number of integration points is limited along the future crack path. Since the crack insertion is delayed due to this limited number of integration points, the peak corresponding to the crack insertion occurs with a delay, which is more pronounced for a coarser mesh, and this induces a snapback yielding the observed oscillations which result from the dynamic integration scheme. Nevertheless, it can be seen that the force response during the crack propagation converges with a refinement of the mesh size and is within the range of experimental curves. Figures 23a and 23b report the distribution of the ligament ratio χ in the deformed configuration respectively at the onset of crack propagation and for an opening $\Delta = 1 \text{ mm}$, in which the crack propagation can also

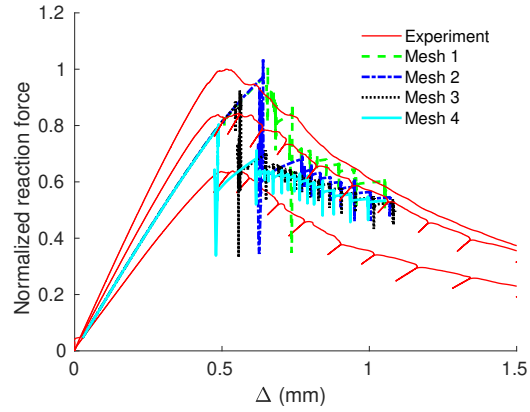


Figure 22: Compact test (CT) specimen: normalized reaction force *vs.* the crack mouth opening Δ for different discretization meshes and comparison with the experimental results.

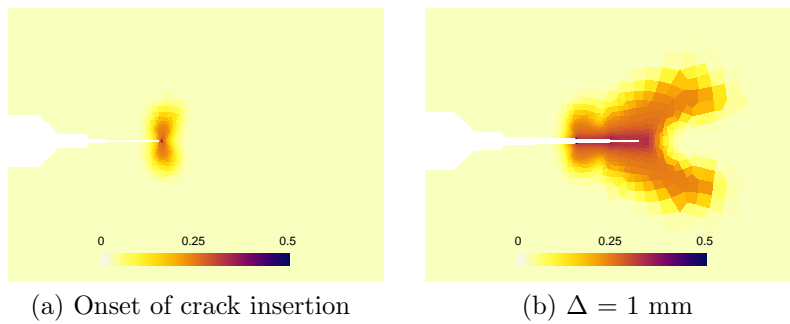


Figure 23: Compact test (CT) specimen: the distribution of the ligament ratio χ in the deformed configuration of Mesh 4 at (a) the onset of crack insertion, and (b) an opening $\Delta = 1$ mm.

be seen.

The damage-to-crack transition is still time consuming. The simulation with the Mesh 4 takes nearly 15 days with a single processor while the simulation with Mesh 1 requires almost two days to be completed. In the future, the computational efficiency needs to be improved. Moreover, the three-dimensional simulations will be considered in order to account for true specimen geometries.

7. Conclusion

This Part II of the work is dedicated to the identification of the porosity-related parameters of the GTN-NH/Thomason model for an HSS material, not only within a fully nonlocal form, but also when relying on a damage-to-crack transition framework. The choice of the GTN-NH/Thomason model allows balancing between strong micromechanics grounds and maintaining an acceptable computational complexity. An efficient identification strategy is proposed, which combines direct material characterization and inverse modeling. The main contributions of the work are the followings:

- The parameters of the porous model are identified using mainly micromechanical argumentation. On the one hand, void cell simulations are exploited to identify the constants q_1 and q_2 of the GTN yield surface and the void spacing growth factor κ by postulating the dissipation equivalence. On the other hand, the characteristic lengths of the coupled nonlocal GTN-NH/Thomason model not only within a fully nonlocal form but also when relying on a damage-to-crack transition framework, are deduced from microstructure characterization.
- Once all the parameters of the GTN-NH/Thomason framework are identified, the model is found to predict correctly the fracture strain evolution for different triaxialities and Lode parameters. However, the cup-cone and the slant fracture paths respectively observed in the round bars and in the plane strain specimens are not correctly predicted by the fully nonlocal GTN-NH/Thomason model, which gives flat fracture paths perpendicular to the loading direction. This arises from the limitation of the GTN-NH/Thomason model in the fracture prediction under shear-dominated loading conditions. Nevertheless, the cup-cone and slant fracture paths can be captured with the use of the damage-to-crack transition framework because of the creation of the free surfaces and the introduction of some scatter of the material parameters, namely the nucleated porosity.

As a matter of fact, other localization mechanisms and criteria come into play in shear-dominated conditions and affect the failure process. In a future work, formalism accounting explicitly for shear-driven coalescence modes [40] will be used to enhance the actual micromechanical description in order to include these additional failure modes.

Acknowledgments

The research has been funded by the Walloon Region under the agreement no.7581-MRIPF in the context of the 16th MECATECH call.

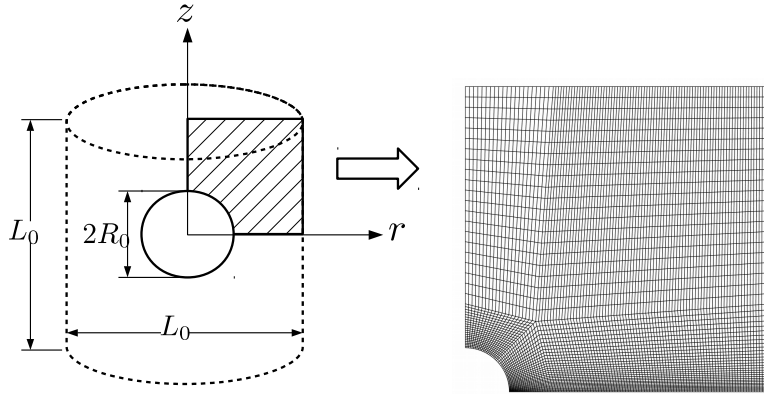


Figure A.24: Axisymmetric cylindrical unit cell (left) and corresponding axisymmetric finite element mesh for $f_{V0} = 2 \times 10^{-3}$ (right).

Data availability

Due to the confidential nature of the research project, participants of this study did not agree for their data to be shared publicly, so supporting data is not available.

Appendix A. Axisymmetric unit cell computation under constant stress triaxiality

A micromechanical analysis is performed on a unit void cell to actually quantify the effect of the stress state on the void growth and coalescence mechanisms similarly to the work of Koplik and Needleman [55] and many others [3, 4, 69]. The overall responses obtained from unit cell simulations are considered as the reference solutions from which the GTN/Thomason parameters, *i.e.* q_1 , q_2 , and κ , can be identified. In this work, an axisymmetric unit cell [29, 57] is considered as shown in Fig. A.24, from which simple finite element simulations under an axisymmetric stress state can be performed. Under an axisymmetric stress state, one has the Lode parameter $\zeta = 1$ following Eq. (18). Consequently, the effect of k_ω in the void growth expression (17) cannot be addressed.

The unit cell consists of a spherical cavity located at its center, see Fig. A.24. Since the material is assumed to be isotropic, the height and the diameter of the cylinder are equal, corresponding to an initial void aspect ratio $\lambda_0 = 1$. The initial porosity f_{V0} and the initial void ligament ratio χ_0 are respectively given as

$$f_{V0} = \frac{2}{3} \left(\frac{2R_0}{L_0} \right)^3 \quad \text{and} \quad \chi_0 = \frac{2R_0}{L_0} = \left(\frac{3}{2} f_{V0} \right)^{\frac{1}{3}}. \quad (\text{A.1})$$

The material of the unit cell is the one of the elastoplastic matrix as described in Eq. (25). Periodic condition implies that the unit cell boundary remains straight [29]. The unit cell simulations are performed for different values of f_{V0} and under different stress triaxiality states. The finite element mesh consists of 9-node axisymmetric quadrilateral elements, see *e.g.* Fig. A.24 (right) where only the case for $f_{V0} = 2 \times 10^{-3}$ is shown.

The resulting macroscopic principal stresses following the axial direction Σ_z and following the radial direction Σ_r are respectively estimated by the average forces at cell boundaries

respectively following z and r (see Fig. A.24) per current area. The equivalent stress measures are computed by

$$p^{\text{cell}} = \frac{1}{3} (\Sigma_z + 2\Sigma_r), \sigma_{\text{eq}}^{\text{cell}} = |\Sigma_z - \Sigma_r|, \text{ and } T^{\text{cell}} = \frac{p^{\text{cell}}}{\sigma_{\text{eq}}^{\text{cell}}}, \quad (\text{A.2})$$

where p^{cell} is the homogenized pressure, $\sigma_{\text{eq}}^{\text{cell}}$ is the homogenized von Mises equivalent stress, and T^{cell} is the macroscopic stress triaxiality, which is equal to the prescribed value T . The current porosity is directly computed from the finite element mesh in the current configuration, such that

$$f_V^{\text{cell}} = \frac{V - \int_{V_0^s} J dV_0}{V}, \quad (\text{A.3})$$

where V is the current cell volume whose initial value is $V_0 = \pi\lambda_0 L_0^3$ and where V_0^s is the initial volume occupied by the solid part. With the use of Eq. (29), the value of ε_m can be estimated since the value of the right hand side term is known.

The arc-length path-following method [70, 71, 72] is used to load the unit cell under a constant stress triaxiality T^{cell} . For the axisymmetric finite element model sketched in Fig. A.24(right), a constant stress triaxiality T^{cell} can be obtained with the following boundary loading conditions:

- bc1) On the axisymmetric (z -) axis: the left edge is horizontally (r -displacement) constrained;
- bc2) Symmetrical boundary condition: the bottom edge is vertically (z -displacement) constrained;
- bc3) Periodic boundary condition implies that the unit cell boundary remains straight [29]: the vertical displacement (z -displacement) of the top edge is uniform and the horizontal displacement (r -displacement) of the right edge is uniform;
- bc4) Pressure boundary condition is applied on the top edge with a value of $-\Sigma_z$;
- bc5) Pressure boundary condition is applied on the right edge with a value of $-\Sigma_r$;

where Σ_z and Σ_r are respectively the principal components of the homogenized stress following respectively the axial direction and the radial direction. Assuming $\Sigma_z > \Sigma_r$, *i.e.* $T^{\text{cell}} \geq 1/3$, in order to facilitate the internal necking mode [29], Eq. (A.2) results into

$$\Sigma_r = \frac{3T^{\text{cell}} - 1}{3T^{\text{cell}} + 2} \Sigma_z. \quad (\text{A.4})$$

As a result, the ratio Σ_r/Σ_z remains constant during the whole loading and depends on the prescribed triaxiality T^{cell} only. Consequently, the boundary value problem is fully controlled by Σ_z since Σ_r is known from the values of Σ_z and T^{cell} . However, since the response of the unit cell exhibits softening, a monotonic pressure increase cannot be used to model the whole loading process, motivating the use of the arc-length path-following method.

Under given f_{V_0} and $T^{\text{cell}} = T$, the results obtained from the unit cell simulations can be expressed as the functions

$$\begin{cases} \sigma_{\text{eq}}^{\text{cell}} &= \sigma_{\text{eq}}^{\text{cell}}(\varepsilon_m; f_{V_0}, T), \text{ and} \\ f_V^{\text{cell}} &= f_V^{\text{cell}}(\varepsilon_m; f_{V_0}, T), \end{cases} \quad (\text{A.5})$$

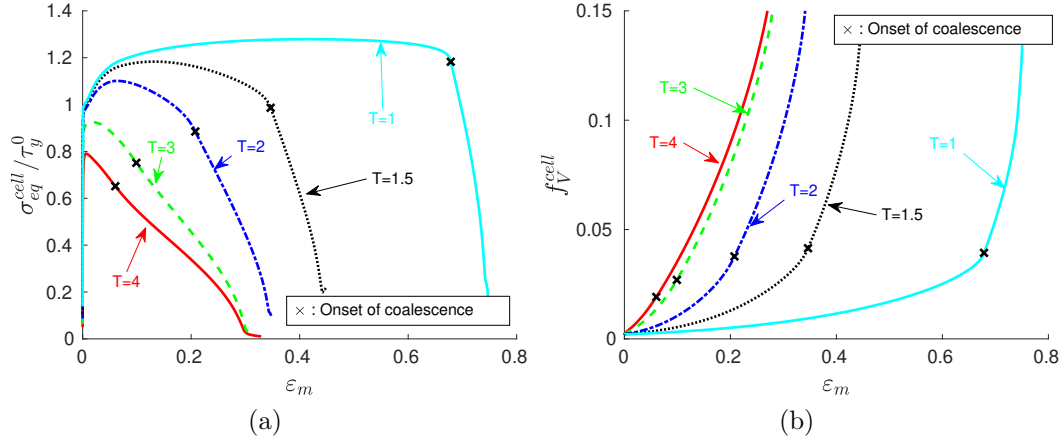


Figure A.25: Unit cell simulations in the case of $f_{V0} = 2 \times 10^{-3}$ for different stress triaxiality states: evolution of the (a) equivalent von Mises stress σ_{eq}^{cell} and (b) porosity f_V^{cell} . The symbol “x” indicates the onset of coalescence.

where ε_m results from the energy equivalence (29). The onset of coalescence occurs when the deformation mode transitions into a uniaxial deformation mode [29, 57]. The values at the onset of coalescence of σ_{eqc}^{cell} and f_{Vc}^{cell} , and ε_{mc}^{cell} are thus easily found. The evolutions of σ_{eq}^{cell} and f_V^{cell} with respect to ε_m are shown in Fig. A.25 for different values of the stress triaxiality and for $f_{V0} = 2 \times 10^{-3}$. The onset of coalescence is also marked. An increase of the stress triaxiality results in a faster void growth and an earlier onset of void coalescence in terms of ε_m .

References

- [1] M. Marteleur, J. Leclerc, M.-S. Colla, V.-D. Nguyen, L. Noels, T. Pardoen, Ductile fracture of high strength steels with morphological anisotropy. part i: Characterization, testing, and void nucleation law, *Engineering Fracture Mechanics* 244 (2021) 107569 (2021). doi:10.1016/j.engfracmech.2021.107569.
- [2] A. A. Benzerga, J.-B. Leblond, Ductile fracture by void growth to coalescence, in: H. Aref, E. van der Giessen (Eds.), *Advances in Applied Mechanics*, Vol. 44 of *Advances in Applied Mechanics*, Elsevier, 2010, pp. 169 – 305 (2010). doi:https://doi.org/10.1016/S0065-2156(10)44003-X. URL <http://www.sciencedirect.com/science/article/pii/S006521561044003X>
- [3] A. A. Benzerga, J.-B. Leblond, A. Needleman, V. Tvergaard, Ductile failure modeling, *International Journal of Fracture* 201 (1) (2016) 29–80 (Sep 2016). doi:10.1007/s10704-016-0142-6. URL <https://doi.org/10.1007/s10704-016-0142-6>
- [4] A. Pineau, A. Benzerga, T. Pardoen, Failure of metals i: Brittle and ductile fracture, *Acta Materialia* 107 (2016) 424 – 483 (2016). doi:https://doi.org/10.1016/j.

- actamat.2015.12.034.
URL <http://www.sciencedirect.com/science/article/pii/S1359645415301403>
- [5] T.-S. Cao, Models for ductile damage and fracture prediction in cold bulk metal forming processes: a review, *International Journal of Material Forming* 10 (2) (2017) 139–171 (Apr. 2017). doi:[10.1007/s12289-015-1262-7](https://doi.org/10.1007/s12289-015-1262-7).
URL <https://hal-mines-paristech.archives-ouvertes.fr/hal-01203082>
- [6] J. Lemaitre, A continuous damage mechanics model for ductile fracture, *Journal of Engineering Materials and Technology* 107 (1) (1985) 83–89 (1985).
- [7] J. Chaboche, M. Boudifa, K. Saanouni, A cdm approach of ductile damage with plastic compressibility, *International Journal of fracture* 137 (1-4) (2006) 51–75 (2006).
- [8] D. J. Celentano, J.-L. Chaboche, Experimental and numerical characterization of damage evolution in steels, *International Journal of Plasticity* 23 (10) (2007) 1739 – 1762, in honor of Professor Dusan Krajcinovic (2007). doi:<https://doi.org/10.1016/j.ijplas.2007.03.008>.
URL <http://www.sciencedirect.com/science/article/pii/S0749641907000484>
- [9] H. Li, M. Fu, J. Lu, H. Yang, Ductile fracture: Experiments and computations, *International Journal of Plasticity* 27 (2) (2011) 147 – 180 (2011). doi:<https://doi.org/10.1016/j.ijplas.2010.04.001>.
URL <http://www.sciencedirect.com/science/article/pii/S0749641910000598>
- [10] T.-S. Cao, J.-M. Gachet, P. Montmitonnet, P.-O. Bouchard, A lode-dependent enhanced lemaître model for ductile fracture prediction at low stress triaxiality, *Engineering Fracture Mechanics* 124-125 (2014) 80 – 96 (2014). doi:<https://doi.org/10.1016/j.engfracmech.2014.03.021>.
URL <http://www.sciencedirect.com/science/article/pii/S0013794414000952>
- [11] F. Yu, M. T. Hendry, S.-X. Li, A stress triaxiality-dependent viscoplastic damage model to analyze ductile fracture under axisymmetric tensile loading, *Engineering Fracture Mechanics* 211 (2019) 99 – 113 (2019). doi:<https://doi.org/10.1016/j.engfracmech.2019.02.014>.
URL <http://www.sciencedirect.com/science/article/pii/S0013794418312396>
- [12] Y. Bao, T. Wierzbicki, A Comparative Study on Various Ductile Crack Formation Criteria , *Journal of Engineering Materials and Technology* 126 (3) (2004) 314–324 (06 2004). arXiv:<https://asmedigitalcollection.asme.org/materialstechnology/article-pdf/126/3/314/5880940/314\1.pdf>, doi:[10.1115/1.1755244](https://doi.org/10.1115/1.1755244).
URL <https://doi.org/10.1115/1.1755244>
- [13] Y. Bai, T. Wierzbicki, A new model of metal plasticity and fracture with pressure and lode dependence, *International Journal of Plasticity* 24 (6) (2008) 1071 – 1096 (2008). doi:<https://doi.org/10.1016/j.ijplas.2007.09.004>.
URL <http://www.sciencedirect.com/science/article/pii/S0749641907001246>

- [14] Y. Bai, T. Wierzbicki, Application of extended mohr–coulomb criterion to ductile fracture, *International Journal of Fracture* 161 (1) (2010) 1 (2010).
- [15] G. Gruben, O. Hopperstad, T. Børvik, Evaluation of uncoupled ductile fracture criteria for the dual-phase steel docol 600dl, *International Journal of Mechanical Sciences* 62 (1) (2012) 133 – 146 (2012). doi:<https://doi.org/10.1016/j.ijmecsci.2012.06.009>. URL <http://www.sciencedirect.com/science/article/pii/S0020740312001452>
- [16] A. L. Gurson, Continuum theory of ductile rupture by void nucleation and growth: Part i - yield criteria and flow rules for porous ductile media, *Journal of Engineering Materials and Technology* 99 (1) (1977) 2–15 (1977).
- [17] V. Tvergaard, A. Needleman, Analysis of the cup-cone fracture in a round tensile bar, *Acta Metallurgica* 32 (1) (1984) 157 – 169 (1984). doi:[https://doi.org/10.1016/0001-6160\(84\)90213-X](https://doi.org/10.1016/0001-6160(84)90213-X). URL <http://www.sciencedirect.com/science/article/pii/000161608490213X>
- [18] A. Needleman, V. Tvergaard, An analysis of ductile rupture in notched bars, *Journal of the Mechanics and Physics of Solids* 32 (6) (1984) 461 – 490 (1984). doi:[https://doi.org/10.1016/0022-5096\(84\)90031-0](https://doi.org/10.1016/0022-5096(84)90031-0). URL <http://www.sciencedirect.com/science/article/pii/0022509684900310>
- [19] C. Chu, A. Needleman, Void nucleation effects in biaxially stretched sheets, *Journal of engineering materials and technology* 102 (3) (1980) 249–256 (1980).
- [20] M. Gologanu, J.-B. Leblond, J. Devaux, Approximate models for ductile metals containing nonspherical voids - case of axisymmetric oblate ellipsoidal cavities, *Journal of Engineering Materials and Technology* 116 (3) (1994) 290–297 (1994).
- [21] M. Gologanu, J.-B. Leblond, J. Devaux, Approximate models for ductile metals containing non-spherical voids - case of axisymmetric prolate ellipsoidal cavities, *Journal of the Mechanics and Physics of Solids* 41 (11) (1993) 1723 – 1754 (1993). doi:[https://doi.org/10.1016/0022-5096\(93\)90029-F](https://doi.org/10.1016/0022-5096(93)90029-F). URL <http://www.sciencedirect.com/science/article/pii/002250969390029F>
- [22] S. Keralavarma, A. Benzerga, A constitutive model for plastically anisotropic solids with non-spherical voids, *Journal of the Mechanics and Physics of Solids* 58 (6) (2010) 874 – 901 (2010). doi:<https://doi.org/10.1016/j.jmps.2010.03.007>. URL <http://www.sciencedirect.com/science/article/pii/S0022509610000682>
- [23] J. Wen, Y. Huang, K. Hwang, C. Liu, M. Li, The modified gurson model accounting for the void size effect, *International Journal of Plasticity* 21 (2) (2005) 381 – 395 (2005). doi:<https://doi.org/10.1016/j.ijplas.2004.01.004>. URL <http://www.sciencedirect.com/science/article/pii/S0749641904000397>
- [24] F. Scheyvaerts, P. Onck, C. Tekoğlu, T. Pardoen, The growth and coalescence of ellipsoidal voids in plane strain under combined shear and tension, *Journal of the Mechanics and Physics of Solids* 59 (2) (2011) 373 – 397 (2011). doi:<https://doi.org/10.1016/>

- j.jmps.2010.10.003.
URL <http://www.sciencedirect.com/science/article/pii/S0022509610002061>
- [25] A. Benzerga, J. Besson, A. Pineau, Anisotropic ductile fracture: Part ii: theory, *Acta Materialia* 52 (15) (2004) 4639 – 4650 (2004). doi:<https://doi.org/10.1016/j.actamat.2004.06.019>.
URL <http://www.sciencedirect.com/science/article/pii/S135964540400357X>
- [26] C. Felipe Guzmán, E. I. Saavedra Flores, A. M. Habraken, Damage characterization in a ferritic steel sheet: Experimental tests, parameter identification and numerical modeling, *International Journal of Solids and Structures* 155 (2018) 109 – 122 (2018). doi:<https://doi.org/10.1016/j.ijsolstr.2018.07.014>.
URL <http://www.sciencedirect.com/science/article/pii/S002076831830297X>
- [27] K. Nahshon, J. Hutchinson, Modification of the gurson model for shear failure, *European Journal of Mechanics - A/Solids* 27 (1) (2008) 1 – 17 (2008). doi:<https://doi.org/10.1016/j.euromechsol.2007.08.002>.
URL <http://www.sciencedirect.com/science/article/pii/S0997753807000721>
- [28] L. Xue, Constitutive modeling of void shearing effect in ductile fracture of porous materials, *Engineering Fracture Mechanics* 75 (11) (2008) 3343 – 3366, local Approach to Fracture (19862006): Selected papers from the 9th European Mechanics of Materials Conference (2008). doi:<https://doi.org/10.1016/j.engfracmech.2007.07.022>.
URL <http://www.sciencedirect.com/science/article/pii/S0013794407003220>
- [29] T. Pardoen, J. Hutchinson, An extended model for void growth and coalescence, *Journal of the Mechanics and Physics of Solids* 48 (12) (2000) 2467 – 2512 (2000). doi:[https://doi.org/10.1016/S0022-5096\(00\)00019-3](https://doi.org/10.1016/S0022-5096(00)00019-3).
URL <http://www.sciencedirect.com/science/article/pii/S0022509600000193>
- [30] P. Thomason, A three-dimensional model for ductile fracture by the growth and coalescence of microvoids, *Acta Metallurgica* 33 (6) (1985) 1087 – 1095 (1985). doi:[https://doi.org/10.1016/0001-6160\(85\)90202-0](https://doi.org/10.1016/0001-6160(85)90202-0).
URL <http://www.sciencedirect.com/science/article/pii/0001616085902020>
- [31] P. Thomason, Three-dimensional models for the plastic limit-loads at incipient failure of the intervoid matrix in ductile porous solids, *Acta Metallurgica* 33 (6) (1985) 1079 – 1085 (1985). doi:[https://doi.org/10.1016/0001-6160\(85\)90201-9](https://doi.org/10.1016/0001-6160(85)90201-9).
URL <http://www.sciencedirect.com/science/article/pii/0001616085902019>
- [32] A. Benzerga, Micromechanics of coalescence in ductile fracture, *Journal of the Mechanics and Physics of Solids* 50 (6) (2002) 1331 – 1362 (2002). doi:[https://doi.org/10.1016/S0022-5096\(01\)00125-9](https://doi.org/10.1016/S0022-5096(01)00125-9).
URL <http://www.sciencedirect.com/science/article/pii/S0022509601001259>
- [33] F. Scheyvaerts, T. Pardoen, P. Onck, A new model for void coalescence by internal necking, *International Journal of Damage Mechanics* 19 (1) (2010) 95–126 (2010). arXiv:

<https://doi.org/10.1177/1056789508101918>, doi:10.1177/1056789508101918.
URL <https://doi.org/10.1177/1056789508101918>

- [34] A. A. Benzerga, J.-B. Leblond, Effective yield criterion accounting for microvoid coalescence, *Journal of Applied Mechanics* 81 (3) (2014) 031009 (2014).
- [35] Z. Zhang, C. Thaulow, J. degrd, A complete gurson model approach for ductile fracture, *Engineering Fracture Mechanics* 67 (2) (2000) 155 – 168 (2000). doi:[https://doi.org/10.1016/S0013-7944\(00\)00055-2](https://doi.org/10.1016/S0013-7944(00)00055-2).
URL <http://www.sciencedirect.com/science/article/pii/S0013794400000552>
- [36] C. F. Guzmán, S. Yuan, L. Duchne, E. I. Saavedra Flores, A. M. Habraken, Damage prediction in single point incremental forming using an extended gurson model, *International Journal of Solids and Structures* 151 (2018) 45 – 56, special Issue with a Selection of Papers from the NUMISHEET 2016 Conference (2018). doi:<https://doi.org/10.1016/j.ijsolstr.2017.04.013>.
URL <http://www.sciencedirect.com/science/article/pii/S0020768317301646>
- [37] A. A. Benzerga, J. Besson, R. Batische, A. Pineau, Synergistic effects of plastic anisotropy and void coalescence on fracture mode in plane strain, *Modelling and Simulation in Materials Science and Engineering* 10 (1) (2002) 73 (2002).
URL <http://stacks.iop.org/0965-0393/10/i=1/a=306>
- [38] J. Besson, Damage of ductile materials deforming under multiple plastic or viscoplastic mechanisms, *International Journal of Plasticity* 25 (11) (2009) 2204 – 2221 (2009). doi:<https://doi.org/10.1016/j.ijplas.2009.03.001>.
URL <http://www.sciencedirect.com/science/article/pii/S0749641909000357>
- [39] J. Leclerc, V.-D. Nguyen, T. Pardoen, L. Noels, A micromechanics-based non-local damage to crack transition framework for porous elastoplastic solids, *International Journal of Plasticity* 127 (2020) 102631 (2020). doi:<https://doi.org/10.1016/j.ijplas.2019.11.010>.
URL <http://www.sciencedirect.com/science/article/pii/S0749641919303821>
- [40] V.-D. Nguyen, T. Pardoen, L. Noels, A nonlocal approach of ductile failure incorporating void growth, internal necking, and shear dominated coalescence mechanisms, *Journal of the Mechanics and Physics of Solids* 137 (2020) 103891 (2020). doi:<https://doi.org/10.1016/j.jmps.2020.103891>.
URL <http://www.sciencedirect.com/science/article/pii/S0022509619309275>
- [41] R. De Borst, L. Sluys, H.-B. Mühlhaus, J. Pamin, Fundamental issues in finite element analyses of localization of deformation, *Engineering computations* 10 (2) (1993) 99–121 (1993).
- [42] M. Jirásek, Nonlocal models for damage and fracture: Comparison of approaches, *International Journal of Solids and Structures* 35 (31) (1998) 4133 – 4145 (1998). doi:[https://doi.org/10.1016/S0020-7683\(97\)00306-5](https://doi.org/10.1016/S0020-7683(97)00306-5).
URL <http://www.sciencedirect.com/science/article/pii/S0020768397003065>

- [43] R. Peerlings, M. Geers, R. de Borst, W. Brekelmans, A critical comparison of nonlocal and gradient-enhanced softening continua, *International Journal of Solids and Structures* 38 (44) (2001) 7723 – 7746 (2001). doi:[https://doi.org/10.1016/S0020-7683\(01\)00087-7](https://doi.org/10.1016/S0020-7683(01)00087-7).
URL <http://www.sciencedirect.com/science/article/pii/S0020768301000877>
- [44] Z. P. Bažant, M. Jirásek, Nonlocal integral formulations of plasticity and damage: survey of progress, *Journal of Engineering Mechanics* 128 (11) (2002) 1119–1149 (2002).
- [45] G. Hütter, T. Linse, U. Mühlich, M. Kuna, Simulation of ductile crack initiation and propagation by means of a non-local gurson-model, *International Journal of Solids and Structures* 50 (5) (2013) 662 – 671 (2013). doi:<https://doi.org/10.1016/j.ijsolstr.2012.10.031>.
URL <http://www.sciencedirect.com/science/article/pii/S0020768312004659>
- [46] Y. Zhang, E. Lorentz, J. Besson, Ductile damage modelling with locking-free regularised gtn model, *International Journal for Numerical Methods in Engineering* 113 (13) (2018) 1871–1903 (2018). arXiv:<https://onlinelibrary.wiley.com/doi/pdf/10.1002/nme.5722>, doi:10.1002/nme.5722.
URL <https://onlinelibrary.wiley.com/doi/abs/10.1002/nme.5722>
- [47] A. Seupel, M. Kuna, A gradient-enhanced damage model motivated by engineering approaches to ductile failure of steels, *International Journal of Damage Mechanics* 28 (8) (2019) 1261–1296 (2019). arXiv:<https://doi.org/10.1177/1056789518823879>, doi:10.1177/1056789518823879.
URL <https://doi.org/10.1177/1056789518823879>
- [48] A. Seupel, G. Htter, M. Kuna, On the identification and uniqueness of constitutive parameters for a non-local gtn-model, *Engineering Fracture Mechanics* 229 (2020) 106817 (2020). doi:<https://doi.org/10.1016/j.engfracmech.2019.106817>.
URL <http://www.sciencedirect.com/science/article/pii/S0013794419306769>
- [49] Y. Chen, E. Lorentz, J. Besson, Crack initiation and propagation in small-scale yielding using a nonlocal gtn model, *International Journal of Plasticity* 130 (2020) 102701 (2020). doi:<https://doi.org/10.1016/j.ijplas.2020.102701>.
URL <http://www.sciencedirect.com/science/article/pii/S0749641919304085>
- [50] S. Baltic, J. Magnien, H.-P. Gnsler, T. Antretter, R. Hammer, Coupled damage variable based on fracture locus: Modelling and calibration, *International Journal of Plasticity* 126 (2020) 102623 (2020). doi:<https://doi.org/10.1016/j.ijplas.2019.11.002>.
URL <http://www.sciencedirect.com/science/article/pii/S0749641919305406>
- [51] R. H. J. Peerlings, R. De Borst, W. A. M. Brekelmans, J. H. P. De Vree, Gradient enhanced damage for quasi-brittle materials, *International Journal for Numerical Methods in Engineering* 39 (19) (1996) 3391–3403 (1996).
URL <http://www.scopus.com/inward/record.url?eid=2-s2.0-0030267284&partnerID=tZ0tx3y1>

- [52] J. Besson, D. Steglich, W. Brocks, Modeling of crack growth in round bars and plane strain specimens, *International Journal of Solids and Structures* 38 (46) (2001) 8259 – 8284 (2001). doi:[https://doi.org/10.1016/S0020-7683\(01\)00167-6](https://doi.org/10.1016/S0020-7683(01)00167-6).
URL <http://www.sciencedirect.com/science/article/pii/S0020768301001676>
- [53] J. Besson, D. Steglich, W. Brocks, Modeling of plane strain ductile rupture, *International Journal of Plasticity* 19 (10) (2003) 1517 – 1541 (2003). doi:[https://doi.org/10.1016/S0749-6419\(02\)00022-0](https://doi.org/10.1016/S0749-6419(02)00022-0).
URL <http://www.sciencedirect.com/science/article/pii/S0749641902000220>
- [54] J. Remmers, R. Borst, de, C. Verhoosel, A. Needleman, The cohesive band model : a cohesive surface formulation with stress triaxiality, *International Journal of Fracture* 181 (2) (2013) 177–188 (2013). doi:[10.1007/s10704-013-9834-3](https://doi.org/10.1007/s10704-013-9834-3).
- [55] J. Koplik, A. Needleman, Void growth and coalescence in porous plastic solids, *International Journal of Solids and Structures* 24 (8) (1988) 835 – 853 (1988). doi:[https://doi.org/10.1016/0020-7683\(88\)90051-0](https://doi.org/10.1016/0020-7683(88)90051-0).
URL <http://www.sciencedirect.com/science/article/pii/0020768388900510>
- [56] J. Faleskog, X. Gao, C. F. Shih, Cell model for nonlinear fracture analysis-i. micromechanics calibration, *International Journal of Fracture* 89 (4) (1998) 355–373 (1998).
- [57] J. Kim, X. Gao, T. S. Srivatsan, Modeling of void growth in ductile solids: effects of stress triaxiality and initial porosity, *Engineering Fracture Mechanics* 71 (3) (2004) 379 – 400 (2004). doi:[https://doi.org/10.1016/S0013-7944\(03\)00114-0](https://doi.org/10.1016/S0013-7944(03)00114-0).
URL <http://www.sciencedirect.com/science/article/pii/S0013794403001140>
- [58] G. Vadillo, J. Reboul, J. Fernandez-Sez, A modified gurson model to account for the influence of the lode parameter at high triaxialities, *European Journal of Mechanics - A/Solids* 56 (2016) 31 – 44 (2016). doi:<https://doi.org/10.1016/j.euromechsol.2015.09.010>.
URL <http://www.sciencedirect.com/science/article/pii/S099775381500131X>
- [59] A. L. Eterovic, K.-J. Bathe, A hyperelastic-based large strain elasto-plastic constitutive formulation with combined isotropic-kinematic hardening using the logarithmic stress and strain measures, *International Journal for Numerical Methods in Engineering* 30 (6) (1990) 1099–1114 (1990). arXiv:<https://onlinelibrary.wiley.com/doi/pdf/10.1002/nme.1620300602>, doi:[10.1002/nme.1620300602](https://doi.org/10.1002/nme.1620300602).
URL <https://onlinelibrary.wiley.com/doi/abs/10.1002/nme.1620300602>
- [60] T. Pardoen, J. Hutchinson, Micromechanics-based model for trends in toughness of ductile metals, *Acta Materialia* 51 (1) (2003) 133 – 148 (2003). doi:[https://doi.org/10.1016/S1359-6454\(02\)00386-5](https://doi.org/10.1016/S1359-6454(02)00386-5).
URL <http://www.sciencedirect.com/science/article/pii/S1359645402003865>
- [61] T. Pardoen, Numerical simulation of low stress triaxiality ductile fracture, *Computers & Structures* 84 (26) (2006) 1641 – 1650 (2006). doi:<https://doi.org/10.1016/j>.

compstruc.2006.05.001.

URL <http://www.sciencedirect.com/science/article/pii/S0045794906001659>

- [62] P. Steinmann, Formulation and computation of geometrically non-linear gradient damage, *International Journal for Numerical Methods in Engineering* 46 (5) (1999) 757–779 (1999).
- [63] M. E. Gurtin, L. Anand, The decomposition $f = f_{\text{efp}}$, material symmetry, and plastic irrotationality for solids that are isotropic-viscoplastic or amorphous, *International Journal of Plasticity* 21 (9) (2005) 1686 – 1719 (2005). doi:<https://doi.org/10.1016/j.ijplas.2004.11.007>.
URL <http://www.sciencedirect.com/science/article/pii/S0749641904001603>
- [64] C. Tekoğlu, J. W. Hutchinson, T. Pardoen, On localization and void coalescence as a precursor to ductile fracture, *Philosophical Transactions of the Royal Society A: Mathematical, Physical and Engineering Sciences* 373 (2038) (2015) 20140121 (2015). arXiv:<https://royalsocietypublishing.org/doi/pdf/10.1098/rsta.2014.0121>, doi:10.1098/rsta.2014.0121.
URL <https://royalsocietypublishing.org/doi/abs/10.1098/rsta.2014.0121>
- [65] F. Beremin, Cavity formation from inclusions in ductile fracture of a508 steel, *Metallurgical Transactions A* 12 (5) (1981) 723–731 (1981).
- [66] G. Perrin, J. Leblond, Analytical study of a hollow sphere made of plastic porous material and subjected to hydrostatic tension-application to some problems in ductile fracture of metals, *International Journal of Plasticity* 6 (6) (1990) 677 – 699 (1990). doi:[https://doi.org/10.1016/0749-6419\(90\)90039-H](https://doi.org/10.1016/0749-6419(90)90039-H).
URL <http://www.sciencedirect.com/science/article/pii/074964199090039H>
- [67] M. G. Geers, R. De Borst, W. A. Brekelmans, R. H. Peerlings, Strain-based transient-gradient damage model for failure analyses, *Computer Methods in Applied Mechanics and Engineering* 160 (1-2) (1998) 133–153 (1998). doi:10.1016/S0045-7825(98)80011-X.
URL <http://www.sciencedirect.com/science/article/pii/S004578259880011X>
- [68] L. H. Poh, G. Sun, Localizing gradient damage model with decreasing interactions, *International Journal for Numerical Methods in Engineering* 110 (6) (2017) 503–522 (2017). arXiv:<https://onlinelibrary.wiley.com/doi/pdf/10.1002/nme.5364>, doi:10.1002/nme.5364.
URL <https://onlinelibrary.wiley.com/doi/abs/10.1002/nme.5364>
- [69] J. Besson, Continuum models of ductile fracture: A review, *International Journal of Damage Mechanics* 19 (1) (2010) 3–52 (2010). arXiv:<https://doi.org/10.1177/1056789509103482>, doi:10.1177/1056789509103482.
URL <https://doi.org/10.1177/1056789509103482>
- [70] E. Riks, An incremental approach to the solution of snapping and buckling problems, *International Journal of Solids and Structures* 15 (7) (1979) 529 – 551 (1979). doi:

[http://dx.doi.org/10.1016/0020-7683\(79\)90081-7](http://dx.doi.org/10.1016/0020-7683(79)90081-7).

URL <http://www.sciencedirect.com/science/article/pii/0020768379900817>

- [71] E. Riks, On formulations of path-following techniques for structural stability analysis, NASA STI/Recon Technical Report N 931 (1992) 16346–+ (Feb. 1992).
- [72] M. G. D. Geers, Enhanced solution control for physically and geometrically non-linear problems. part ii comparative performance analysis, International Journal for Numerical Methods in Engineering 46 (2) (1999) 205–230 (1999). doi:10.1002/(SICI)1097-0207(19990920)46:2<205::AID-NME669>3.0.CO;2-S.
URL [http://dx.doi.org/10.1002/\(SICI\)1097-0207\(19990920\)46:2<205::AID-NME669>3.0.CO;2-S](http://dx.doi.org/10.1002/(SICI)1097-0207(19990920)46:2<205::AID-NME669>3.0.CO;2-S)